Computers and Geotechnics 150 (2022) 104888

Contents lists available at ScienceDirect

Computers and Geotechnics

journal homepage: www.elsevier.com/locate/compgeo

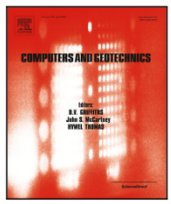

Research paper

A consistent calibration process for the Matsuoka–Nakai friction angle under direct simple shear conditions for clay hypoplasticity

Gertraud Medicus [a,*], Katherine A. Kwa [b], Benjamin Cerfontaine [b]

[a] University of Innsbruck, Austria
[b] University of Southampton, UK

ARTICLE INFO

MSC:
00-01
99-00

Keywords:
Hypoplasticity
Matsuoka–Nakai
Clay
Direct simple shear
Critical state

ABSTRACT

In geotechnical engineering, direct simple shear (DSS) tests are used to determine strength and stiffness parameters of a material. DSS predictions of a constitutive model influence failure mechanisms in plane-strain, finite-element applications. In this article, we introduce a closed-form solution to determine the Matsuoka–Nakai equivalent critical friction angle from direct simple shear stress and normal stress data. In order to apply it to clay hypoplasticity (Mašín, 2013), we carry out DSS simulations to investigate rotations of principal stresses and the principal stress state at critical state for plane-strain conditions.

Finally, we interpret DSS predictions of clay hypoplasticity for different overconsolidation ratios and demonstrate that the location of the CSL in the vertical stress–void ratio plane coincides with the location of the CSL in mean effective stress–void ratio plane.

1. Introduction

Modern offshore foundation design relies increasingly on numerical modelling of soil-foundation interactions (Liu et al., 2021; Byrne et al., 2020; Page et al., 2021). Therefore, constitutive models must be able to reproduce realistic complex stress states and histories that develop around foundations, and model parameters must be calibrated against typical experimental element tests undertaken by industry.

Calibration and predictions of constitutive models are often investigated by axisymmetric element test simulations, such as conventional undrained and drained triaxial compression/extension tests, at various initial void ratios and stress states, e.g. von Wolffersdorff (1996), Taiebat and Dafalias (2008) and Wichtmann (2020). In these cases, the deformation is only rectilinear (*in-axis-deformation*), i.e. there is no change in the direction of principal stresses. For instance, such predictions of clay hypoplasticity have been extensively carried out by Gudehus and Mašín (2009), Mašín and Herle (2005, 2007) and Mašín (2019, 2013).

In the offshore geotechnical practice, the direct simple shear (DSS) test is an established experiment that is commonly used in site investigation to determine geotechnical parameters cf. Dyvik et al. (1987) and Randolph (2000). This is because the DSS test is a relatively accessible laboratory element test and cost-effective alternative to full-scale onsite testing or scale modelling techniques which also characterize the geotechnical response around foundations.

The DSS test applies simple shear conditions to a soil specimen where it is consolidated under one-dimensional conditions and then sheared, allowing for shear distortion in only one-direction. DSS tests are often performed to determine soil parameters related to potential failure surfaces because the soil along the failure surface around the soil-foundation interaction zone when the foundation is subjected to combined loading, is close to DSS conditions. DSS tests also produce an intermediate soil strength between triaxial compression and extension, which is appropriate for when a single measured value is to be used for practical assessment of foundation capacity, cf. Dyvik et al. (1987), Mayne (1985), Kinner (1973), Randolph (2000) and Andersen (2009).

A simple shear test is deformed under plane-strain deformation, which is not rectilinear, because rotations of principal stresses occur, e.g. Kolymbas and Herle (2003). For instance, in sand hypoplasticity by von Wolffersdorff (1996), the inclination of major principal stress to the horizontal direction is approximately 45° at the critical state, as investigated by Schranz and Fellin (2015) and Schranz (2018). This implies that the horizontal plane in the DSS test is the plane where the shear stress τ is maximal, which is in accordance with DEM simulations by Zhang (2003) and Thornton and Zhang (2006) cf. Yu (2006). Bernhardt-Barry et al. (2021) confirm this assumption for loose samples through their DEM simulations. However, Wijewickreme et al. (2013) carried out DEM simulations where they showed that the horizontal plane is the plane where the stress ratio τ/σ_v' is a maximum

* Corresponding author.
E-mail address: gertraud.medicus@uibk.ac.at (G. Medicus).

https://doi.org/10.1016/j.compgeo.2022.104888
Received 12 December 2021; Received in revised form 21 June 2022; Accepted 23 June 2022
Available online 6 July 2022

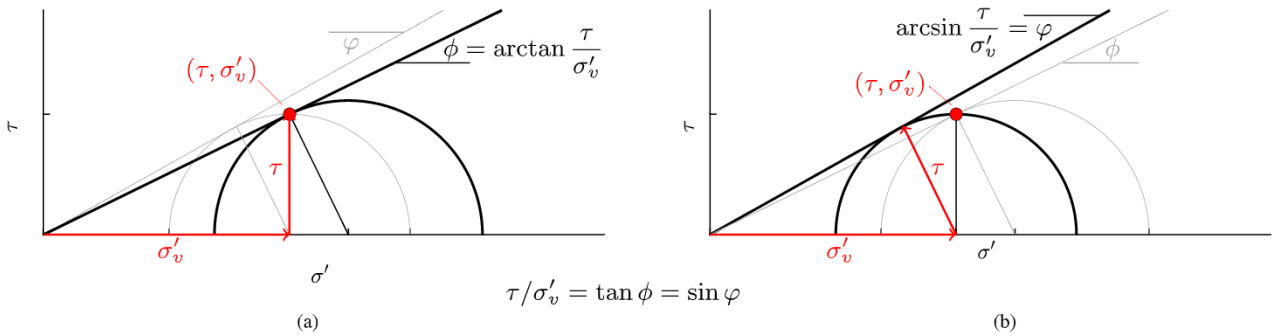

Fig. 1. For a pair of τ and σ'_v (red bullet), the related Mohr circle is unknown (with two possible Mohr circles shown here) and thus the determination of the friction angle is not unique. Figs. (a) and (b) show two prevalent possibilities (bold lines) for the determination of the Mohr–Coulomb friction angles ϕ and φ. Fig. (a) shows the approach displayed in (b) in thin grey lines and vice versa.
Source: Figure modified from Rowe (1969), Atkinson et al. (1991) and Thornton and Zhang (2006).

at large strains. Both prevalent assumptions are displayed in Fig. 1. Therefore, the calibration of parameters, such as the friction angle, may not be unequivocally determined, see Rowe (1969), Atkinson et al. (1991) and Thornton and Zhang (2006).

Furthermore, even if the stress rotation is known, the shear and normal stresses measured from conventional DSS experiments are not sufficient to completely describe the principal stress state of a material, as the out of plane stress is usually not measured. A DSS test is deformed under plane-strain conditions, and causes a specific type of non-axisymmetric, non-rectilinear stress path, that can be displayed in principal stress space and there is a range in the Lode angle θ, which describes plane-strain failure. For example, stress paths of normally consolidated soil under plane-strain failure are reported to lie within $0° \leq \theta \leq 15°$ according to Nakai (2007), and Potts and Zdravković (1999) report $10° \leq \theta \leq 22°$ under plane strain conditions for biaxial tests on clays.

In elastoplastic models, the Lode angle θ at plane-strain failure is dependent on the shape of the plastic potential surface, cf. Potts and Zdravković (1999), Grammatikopoulou et al. (2007), Lagioia and Panteghini (2014) and Sławińska-Budzich (2021). For example in a linear-elastic, perfectly-plastic model, which uses Mises as plastic potential surface, the Lode angle $\theta = 0°$ is reached at plane-strain failure, see Tsegaye et al. (2013) and Lagioia and Panteghini (2014). However, for other shapes of plastic potential surfaces, different Lode angles at plane-strain failure can be obtained, also for models that include the Matsuoka–Nakai failure criterion and plastic potential surface, see Lagioia and Panteghini (2014). The surface according to Matsuoka and Nakai (1982) takes into account the influence of intermediate principal stress and is incorporated in some constitutive models, e.g. von Wolffersdorff (1996), Nakai and Hinokio (2004), Kolymbas (2015), Mašín (2013) and Medicus and Fellin (2017). For the constitutive model barodesy for clay (Medicus and Fellin, 2017), the Lode angle under plane strain conditions is friction dependent and lies between 5° and 15°, see also Medicus (2020).

Consequently, in order to use DSS experimental results to calibrate constitutive model parameters, it is important to understand how the adopted constitutive model captures DSS behaviour and how the combined effects of principal stress rotation and plane-strain conditions affect the model's calibration procedure.

The novelties of this paper are:

1. We introduce two analytical, Lode angle dependent approaches to determine the Matsuoka–Nakai equivalent critical friction angle from direct simple shear stress and normal stress data. To this end, we employ the assumptions as displayed in Fig. 1 to Matsuoka–Nakai.
2. In order to apply the approaches to clay hypoplasticity according to Mašín (2013), we investigate rotations of principal stresses and the principal stress state at critical state of the hypoplastic model.
3. We further demonstrate that the mean effective stress equals the vertical stress under critical state DSS conditions for the hypoplastic model. Demonstrating this, allows us to formulate the Critical State Line in void ratio–vertical effective stress plane.

In addition, our investigations aim to improve the understanding of simple shear simulations related to clay hypoplasticity and enable an interpretation within Critical State Soil Mechanics. We further evaluate stress paths in principal stress space, investigate different overconsolidation ratios and evaluate and interpret possible soil states in the framework of Critical State Soil Mechanics. The outcomes of this studies can therefore also be relevant for plane-strain applications of clay hypoplasticity as carried out by e.g. Nitzsche and Herle (2014), Stutz et al. (2017), Kadlíček and Mašín (2020) and Jerman and Mašín (2021). For a summary of the *symbols and notation* that we have adopted, please refer to Appendix A.

2. Determination of friction angles from DSS critical state data

In this section, we describe conventional possibilities to determine friction angles under direct shear condition when assuming Mohr–Coulomb failure. For a pair of τ and σ'_v at critical state, the related Mohr circle is unknown and thus the determination of the friction angle is not unique, e.g. Rowe (1969), Atkinson et al. (1991), Zhang (2003), Thornton and Zhang (2006), Wijewickreme et al. (2013) and Schranz and Fellin (2015). In this article, because we focus on critical strength prediction, we set cohesion c to zero.

Fig. 1 shows two prevalent possibilities for the determination of a Mohr–Coulomb friction angle for a given pair of τ and σ'_v from a DSS experiment:

(a) If τ and σ'_v describes the tangent point on the Mohr–Coulomb tangent line, the horizontal plane in the DSS test is the plane where the *stress ratio* τ/σ'_v is maximal and ϕ is determined from $\phi = \arctan(\tau/\sigma'_v)$, see thick line in Fig. 1(a). DEM simulations of DSS tests by Wijewickreme et al. (2013) support this assumption.

(b) If the pair of τ and σ'_v describes the highest point on the Mohr circle, the horizontal plane in the DSS test is the plane where the *shear stress* τ is maximal, see thick line Fig. 1(b). This implies that the inclination of major principal stress to the horizontal direction equals 45° and φ can be determined from

$$\sin\varphi = \tau/\sigma'_v \quad . \tag{1}$$

At critical state (no further change in volume), the coaxiality of the stress tensor and strain increment tensor is given, see also Wood (2004). This indicates that the assumption in Fig. 1(b) is plausible for critical states. In addition, DEM investigations by Thornton and Zhang (2006) and Bernhardt-Barry et al. (2021) support this assumption and to determine the Mohr–Coulomb friction angle φ.

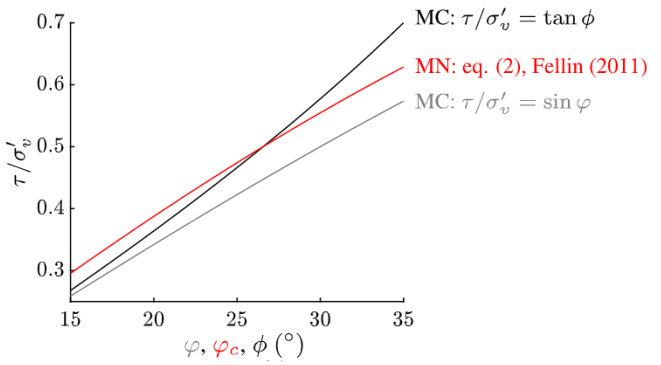

Fig. 2. DSS stress ratio τ/σ'_v in dependence of ϕ and φ as defined in Fig. 1, and φ_c.

The Mohr–Coulomb friction angle can be uniquely determined once the direction and magnitude of principal stresses are known. However, some other surfaces (e.g. Matsuoka–Nakai) include a strength dependency to the intermediate principal stress σ'_2 and the Mohr–Coulomb friction angle cannot be applied directly.

Fellin (2011) therefore proposes a kinematic solution, which results in the following relationship between the Matsuoka–Nakai friction angle φ_c and Mohr–Coulomb friction angle ϕ under simple shear conditions:

$$\sin\varphi_c = \frac{\sqrt{18\cos^2\phi - 15\cos^4\phi - 3}}{5\cos^2\phi - 1} \quad \text{with} \quad \phi = \arctan\frac{\tau}{\sigma'_v} \tag{2}$$

Fig. 2 shows the DSS stress ratio τ/σ'_v in dependence of the Mohr–Coulomb friction angles ϕ and φ and the Matsuoka–Nakai friction angle φ_c.

3. Calibration of the Matsuoka–Nakai (MN) equivalent friction angle under DSS conditions

In this section, we introduce Lode angle dependent, analytical approaches to determine Matsuoka–Nakai friction angles from DSS τ and σ'_v data. Matsuoka–Nakai takes into account the intermediate principal stress $\sigma'_2 = (1-b)\sigma'_3 + b\sigma'_1$, which is $\sigma'_3 \le \sigma'_2 \le \sigma'_1$ for $0 \le b \le 1$. Thus, b defines the deviatoric direction of a principal stress state with $b = \frac{\sigma'_3 - \sigma'_2}{\sigma'_3 - \sigma'_1}$ where $b = 0$ corresponds to axisymmetric compression (i.e. a Lode angle $\theta = 30°$) and $b = 1$ corresponds to axisymmetric extension ($\theta = -30°$). Non-axisymmetric states are characterized by $0 < b < 1$ and $-30° < \theta < 30°$. For example $b = 1/2$ corresponds to $\theta = 0°$. Therefore, the Lode angle as a function of b is $\theta = \arctan\left(\frac{1-2b}{\sqrt{3}}\right)$.

As described in Section 2, the principal stress state for a pair of DSS τ and σ'_v is unknown and different assumptions can be applied. For the determination of the Matsuoka–Nakai friction angle, we will again apply the two assumptions, that the horizontal plane in the DSS test is the plane where either (a) the stress ratio τ/σ'_v is maximal or (b) the shear stress τ is maximal at critical state, see Fig. 3. For case (a), the Matsuoka–Nakai equivalent friction angle is labelled ϕ_c, for case (b) we use φ_c. The Matsuoka–Nakai failure surface in terms of principal stresses reads, see also Matsuoka and Nakai (1982) and Griffiths and Huang (2009):

$$\frac{(\sigma'_1\sigma'_2 + \sigma'_2\sigma'_3 + \sigma'_3\sigma'_1)(\sigma'_1 + \sigma'_2 + \sigma'_3)}{\sigma'_1\sigma'_2\sigma'_3} = K_{\mathrm{MN}} \tag{3}$$

with

$$K_{\mathrm{MN}} = \frac{9 - \sin^2\phi_c}{1 - \sin^2\phi_c} \quad . \tag{4}$$

for the assumption displayed in Fig. 3(a) and

$$K_{\mathrm{MN}} = \frac{9 - \sin^2\varphi_c}{1 - \sin^2\varphi_c} \quad . \tag{5}$$

for the assumption displayed in Fig. 3(b). For the determination of the Matsuoka–Nakai friction angle, we formulate the principal stresses σ'_1, σ'_2 and σ'_3 in terms of τ and σ'_v and the Lode angle θ.

(a) In Fig. 3(a), the stress ratio τ/σ_v is again assumed to be maximal on the horizontal plane of a DSS test, see also Fig. 1(a). The centre of the Mohr circle is then $m = \sigma'_v + \tau\tan\phi$ and with $\tan\phi = \tau/\sigma'_v$, $m = \sigma'_v + \tau^2/\sigma'_v$. The radius r is $\tau/\cos\phi$ and with $\cos\phi = \frac{1}{\sqrt{\frac{\tau^2}{\sigma'^2_v}+1}}$, it follows that $r = \tau\sqrt{\frac{\tau^2}{\sigma'^2_v}+1}$. The principal stresses under DSS critical state conditions can therefore be formulated as follows:

$$\sigma'_1 = m + r = \sigma'_v + \frac{\tau^2}{\sigma'_v} + \tau\sqrt{\frac{\tau^2}{\sigma'^2_v}+1} \tag{6}$$

$$\sigma'_2 = m + r(2b-1) = \sigma'_v + \frac{\tau^2}{\sigma'_v} + \tau\sqrt{\frac{\tau^2}{\sigma'^2_v}+1}(2b-1) \tag{7}$$

$$\sigma'_3 = m - r = \sigma'_v + \frac{\tau^2}{\sigma'_v} - \tau\sqrt{\frac{\tau^2}{\sigma'^2_v}+1} \tag{8}$$

With σ'_1, σ'_2 and σ'_3 from Eqs. (6), (7), (8) in Eqs. (3) and (4), ϕ_c in terms of τ, σ'_v and b can be formulated:

$$\sin\phi_c = \sqrt{\frac{\tau^2\left(y\sigma'^2_v + y\tau^2 + z\right)}{x\left(\sigma'^2_v + y\tau^2 + z\right)}} \tag{9}$$

with $x = \sigma'^2_v + \tau^2$, $y = b^2 - b + 1$, $z = (2b-1)\sigma'_v\tau\sqrt{\frac{\tau^2}{\sigma'^2_v}+1}$. Therefore, for a given value of b that corresponds to plane strain failure of a constitutive model, the Matsuoka–Nakai friction angle can be determined from DSS data τ and σ'_v. Setting $b = 1/2$ in Eq. (9), the following ϕ_c is obtained from DSS data τ and σ'_v for a constitutive model that reaches the Lode angle $\theta = 0°$ at critical state:

$$\sin\phi_c = \frac{\sqrt{3\sigma'^2_v\tau^2 + 3\tau^4}}{\sqrt{4\sigma'^4_v + 7\sigma'^2_v\tau^2 + 3\tau^4}} \tag{10}$$

Alternatively, τ/σ'_v as a function of ϕ_c for $b = 1/2$ can be formulated. The DSS stress ratio τ/σ'_v is then:

$$\frac{\tau}{\sigma'_v} = \frac{2\sin\phi_c}{\sqrt{3(1-\sin\phi_c^2)}} \tag{11}$$

In Fig. 4(a), the result of applying Eq. (9) for different values of b, respectively θ = const, is visualized. The value of ϕ_c can be determined from the DSS stress ratio τ/σ'_v for a given value of θ that corresponds to plane strain critical state. For a given τ/σ'_v, the resulting ϕ_c is similar in the range of $0° < \theta < 20°$. Note that Eqs. (6), (7), (8), (10), (11) refer to the assumption that the horizontal plane in the DSS test is the plane where the stress ratio τ/σ'_v is maximal, see also Figs. 3 (a) and 4 (a).

(b) As described in Section 2, it can as well be assumed that the horizontal plane in the DSS test is the plane where the shear stress τ is maximal, see Figs. 1(b) and 3(b). The inclination of major principal stress to the horizontal direction is then equal 45°. The intermediate principal stress σ'_2 is $\sigma'_3 \le \sigma'_2 \le \sigma'_1$. The principal stresses under DSS critical state conditions can therefore be formulated as follows:

$$\sigma'_1 = \sigma'_v + \tau \tag{12}$$

$$\sigma'_2 = \sigma'_v + \tau(2b-1) \tag{13}$$

$$\sigma'_3 = \sigma'_v - \tau \tag{14}$$

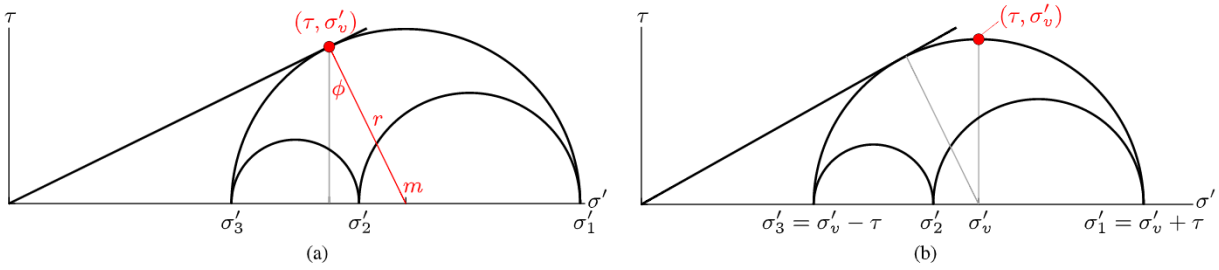

Fig. 3. For the determination of the Matsuoka–Nakai friction angle the principal stress states are expressed in terms of τ, σ'_v and b: In Fig. (a) the stress ratio τ/σ'_v is assumed to be maximal, see also Fig. 1(a). In Fig. (b) the shear stress τ is assumed to be maximal, see also Fig. 1(b). The intermediate principal stress in case (b) is $\sigma'_2 = \sigma'_v + \tau(2b-1)$.

With σ'_1, σ'_2 and σ'_3 from Eqs. (12), (13), (14) in Eqs. (3) and (5), results in φ_c in terms of τ, σ'_v and b:

$$\sin\varphi_c = \frac{2\sqrt{2}\tau\sqrt{\sigma'_v - b\sigma'_v + b^2\sigma'_v - \tau + 2b\tau}}{\sqrt{8\sigma_v^3 - 8\sigma_v^2\tau + 16b\sigma_v^2\tau - 8b\sigma'_v\tau^2 + 8b^2\sigma'_v\tau^2}} \tag{15}$$

Therefore, for a given value of b that corresponds to plane strain failure of a constitutive model, the Matsuoka–Nakai equivalent friction angle can be determined from DSS τ and σ'_v data. Setting $b = 1/2$ in Eq. (15), we obtain:

$$\sin\varphi_c = \sqrt{\frac{3\tau^2}{4\sigma'^2_v - \tau^2}} \tag{16}$$

Alternatively, τ/σ'_v in dependence of φ_c for $b = 1/2$ can be formulated. The DSS stress ratio for a constitutive model that reaches the Lode angle $\theta = 0°$ at critical state is then:

$$\frac{\tau}{\sigma'_v} = \sqrt{\frac{4\sin^2\varphi_c}{3 + \sin^2\varphi_c}} \tag{17}$$

Eq. (17) is a special case of the Lode angle dependent solution according to Eq. (15) and coincides with the kinematic solution according to Eq. (2), as proposed by Fellin (2011). In Fig. 4(b), the result of applying Eq. (15) for different values of b, respectively θ =const, is visualized. For a given value of θ that corresponds to plane strain critical state, φ_c can be determined from the DSS stress ratio τ/σ'_v. For a given τ/σ'_v, the resulting φ_c is similar in the range of $0° < \theta < 20°$. The results of Fig. 4(a) are displayed in (b) with thin grey lines. For example for a given stress ratio $\tau/\sigma'_v = 0.49$ and a Lode angle of $\theta = 0°$ (solid lines), the resulting Matsuoka–Nakai friction angles are $\phi_c = 23°$ (Eq. (10)) and $\varphi_c = 26°$ (Eq. (16)). The difference between ϕ_c and φ_c is smaller for lower friction angles and more pronounced for larger friction angles: For a given stress ratio of $\tau/\sigma'_v = 0.63$ and a Lode angle of $\theta = 0°$, the resulting Matsuoka–Nakai friction angles are $\phi_c = 28.6°$ and $\varphi_c = 35°$.

For a consistent calibration of the Matsuoka–Nakai friction angle from DSS data, (i) the Lode angle as well as (ii) the stress rotation at plane strain critical state have to be identified. We therefore investigate clay hypoplasticity according to Mašín (2013) with respect these aspects, in order to apply a consistent calibration for the Matsuoka–Nakai equivalent friction angle.

4. Simulations of monotonic DSS tests with clay hypoplasticity

In this section drained and undrained simple shear tests are simulated with clay hypoplasticity and evaluated in the framework of Critical State Soil Mechanics. The equations of hypoplasticity are implemented in a set of MATLAB routines using a forward Euler integration scheme. This scheme is accurate enough provided the strain steps are sufficiently small.

Table 1
Parameters of Kaolin calibrated for clay hypoplasticity.

φ_c	N	λ^*	κ^*	ν
25.9°	1.26	0.09	0.01	0.3

4.1. Clay hypoplasticity

Hypoplasticity, introduced by Kolymbas (1977), is a constitutive framework that differs from conventional elasto-plastic models: it does not distinguish between elastic and plastic strain and does not require expressions such as yield function, plastic potential or flow rule. The stress rate is formulated as a tensorial function of the current stress, stretching and the void ratio, i.e. $\mathring{\boldsymbol{\sigma}} = \mathbf{h}(\boldsymbol{\sigma}, \mathbf{D}, e)$, e.g. von Wolffersdorff (1996) and Mašín (2013). Clay hypoplasticity by Mašín (2013) takes into account asymptotic states (Mašín, 2012) as critical states, the influence of stress level (barotropy) and density (pyknotropy). The concepts from Critical State Soil Mechanics that are included in clay hypoplasticity and are relevant to this work, are summarized in Appendix B. The parameters used for the simulations are summarized in Table 1.

4.2. Oedometric normally consolidated K_0 state

If the initial state in the simple shear simulations is oedometrically normally consolidated, K_0 follows Jáky's predictions with $K_0 = 1 - \sin\varphi_c$, which is included in the hypoplastic model. The overconsolidation ratio $\mathrm{OCR} = p'_e/p'$ of normally consolidated/asymptotic states is included in Eq. (18), cf. Mašín (2013):

$$\mathrm{OCR} = \frac{p'_e}{p'} = \frac{1}{\left(1 - \sin^2\varphi_m\right)^{1/\omega}} \tag{18}$$

with

$$\omega = -\frac{\ln(\cos^2\varphi_c)}{\ln 2} + a(\sin^2\varphi_m - \sin^2\varphi_c) \quad . \tag{19}$$

where the critical friction angle φ_c and the parameter a influence the shape of the asymptotic state boundary surface (ASBS). The parameter, a, is set to the default value of 0.3 in all simulations as proposed by Mašín (2013). For oedometric conditions OCR in Eq. (18) is $\mathrm{OCR}_{\mathrm{oed}}$ with φ_m from:

$$\sin\varphi_m = \frac{1 - K_0}{1 + K_0} \quad . \tag{20}$$

In clay hypoplasticity, it is possible to prescribe an initial OCR or an initial void ratio. Prescribing an initial OCR enables the selection of a starting point in the analysis that is consistent with loading history. Therefore we used the latter procedure and fixed an initial OCR in our analyses (as described in the following section) to fit and calibrate the modelled behaviour with experimental results.

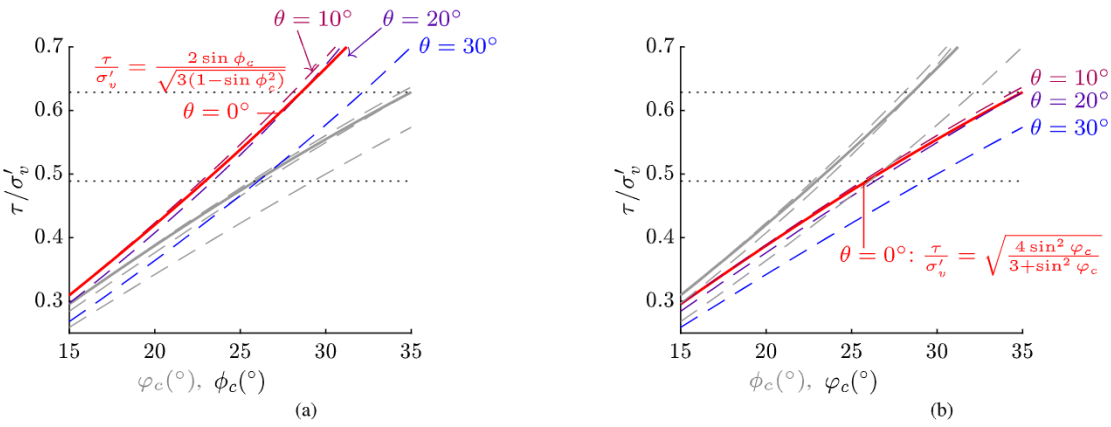

Fig. 4. For a given value of b or θ that corresponds to plane strain critical state, the Matsuoka–Nakai equivalent friction angle can be determined from the DSS stress ratio τ/σ'_v. (a) refers to Eq. (9), i.e. the assumption that the stress ratio τ/σ'_v is assumed to be maximal and the results in (b) refer to Eq. (15), i.e. the assumption that the shear stress τ is maximal at critical state. The results of (a) are displayed in (b) with grey lines and vice versa. The dotted lines refer to $\tau/\sigma'_v = 0.49$ and $\tau/\sigma'_v = 0.63$.

4.3. Interpretation and calibration within critical state soil mechanics

The full calibration procedure is based on an undrained simple shear test as well as on an oedometric compression test. For the parameters N, λ^*, κ^*, we apply the calibration procedure proposed by Mašín (2019), Kadlíček (2019) and Kadlíček et al. (2022) based on an oedometric compression test and refer to Appendix C. The novelty of this work is in the calibration of φ_c within clay hypoplasticity, from DSS experimental data. We further investigate and interpret the DSS predictions within Critical State Soil Mechanics.

Fig. 5 shows a simulation of a simple shear test of an oedometric normally consolidated sample. The initial state of the direct simple shear experiment M90 is reported to be oedometric normally consolidated according to Laham et al. (2021). In Fig. 5 (a), the evolution of the shear stress τ is plotted over the shear strain γ (in radians). Fig. 5 (b) shows the $\tau - \sigma'$ plot. In both plots experimental DSS data is added.

In the experiment M90, the preconsolidation normal stress coincided with the initial normal stress $\sigma'_v = 90\,\text{kPa}$. In our simulation we thus prescribed the OCR and chose the corresponding initial oedometric normally consolidated OCR_{oed} equal to 1.35 according to Eqs. (18)–(20). Note that we therefore adjusted the initial void ratio from the experiment from $e_{\text{ini}} = 1.24$ as reported by Laham et al. (2021) to $e_{\text{ini}} = 1.36$, in order to start at oedometric normally consolidated K_0 state in clay hypoplasticity. Such a void ratio adjustment procedure is common and also applied in the calibration software ExCalibre by Kadlíček et al. (2022) and Kadlíček (2019). The calculated initial void ratio of the DSS specimen was very sensitive to the measured sample height. The void ratio adjustment required to shift the simulated initial state of the sample onto the normal compression line corresponded to a small (5% or 3 mm) increase in sample height, which is within experimental measurement uncertainties that develop from sample disturbance and seating issues during the preparation and assembly stages.

4.3.1. Rotation of principal stresses

In Fig. 5(c), the inclination of major principal stress to the horizontal direction is described by the angle α_σ: The major principal stress direction α_σ is 90° at zero shear strain and decreases with ongoing shear strain. α_σ is then approximately 45° at critical state, i.e. on a horizontal plane that corresponds to maximum shear stress as displayed in Fig. 5(b). At the critical state, the exact value of α_σ is 45.6° for the parameters according to Table 1, independent of the initial stress state and initial density. α_σ slightly decreases for smaller critical friction angles and increases for higher φ_c as displayed in Fig. 6(a), with the other parameters according to the values defined in Table 1. The parameter N has no influence on α_σ at critical state, see Fig. 6 (b). Changes in λ^* also do not have a significant effect on α_σ, see Fig. 6 (c). Increasing κ^* and λ^*, result in higher values of α_σ as displayed in Fig. 6(d), (e).[1]

Note that α_σ is exactly 45° when the Zaremba/Jaumann expression $-\mathbf{W}\boldsymbol{\sigma} + \mathbf{W}\boldsymbol{\sigma}$ is not included in the formulation, i.e. $\dot{\boldsymbol{\sigma}} = \mathring{\boldsymbol{\sigma}}$. This is consistent with Kolymbas and Herle (2003) as they observed that the difference between $\dot{\boldsymbol{\sigma}}$ and $\mathring{\boldsymbol{\sigma}}$ is generally small and only minor differences result in the value of α_σ if the Zaremba/Jaumann expression is included.

(i) Therefore, as the inclination of major principal stress to the horizontal direction is close to 45°, 45° is chosen as approximation in this work. This yields that $\sigma'_v = \left(\sigma'_1 + \sigma'_3\right)/2$.

Point (i) applies for a broad range of material parameters (see Fig. 6 for parametric study), independent of initial conditions. The inclination of major principal stress to the horizontal direction of 45° at critical state leads to the Lode angle dependent formulation of the Matsuoka–Nakai friction angle φ_c according to Eq. (15), see also Figs. 3 (b) and 5 (b).[2]

4.3.2. Plane-strain predictions

The sample in a simple shear test follows a plane-strain deformation. Therefore, the following applies for clay hypoplasticity:

(ii) Evaluating the stress path in principal stress space shows that it reaches a Lode angle $\theta = 0°$ ($b = 1/2$) at critical stress state resulting from the plane-strain constraint. A Lode angle of $\theta = 0°$ implies $\sigma'_2 = (\sigma'_1 + \sigma'_3)/2$, see Fig. 5 (d).

Point (ii) applies for any plane-strain, critical stress prediction with clay hypoplasticity and is thus independent of material parameters as well as it is independent of initial conditions.

4.3.3. Determination of φ_c

With $\theta = 0°$ (i.e. $b = 1/2$) in the general solution according to Eq. (15), φ_c can be unequivocally determined from the shear τ and normal stresses σ'_v measured under DSS conditions at the critical state:

$$\varphi_c = \arcsin\left(\sqrt{\frac{3\tau^2}{4\sigma'^2_v - \tau^2}}\right) \tag{21}$$

Therefore, setting φ_c to the value determined in Eq. (21) results in a consistent critical stress ratio τ/σ'_v between experimental DSS data and hypoplastic simulations. With the calibration according to Eq. (21), the

[1] Choosing $\varphi_c = 35°$, $\lambda^* = 0.15$, κ^*, $\nu = 0.4$ results in $\alpha_\sigma = 47.2°$.

[2] For a MC material, the friction angle φ is obtained from Eq. (1), see also Fig. 1(b).

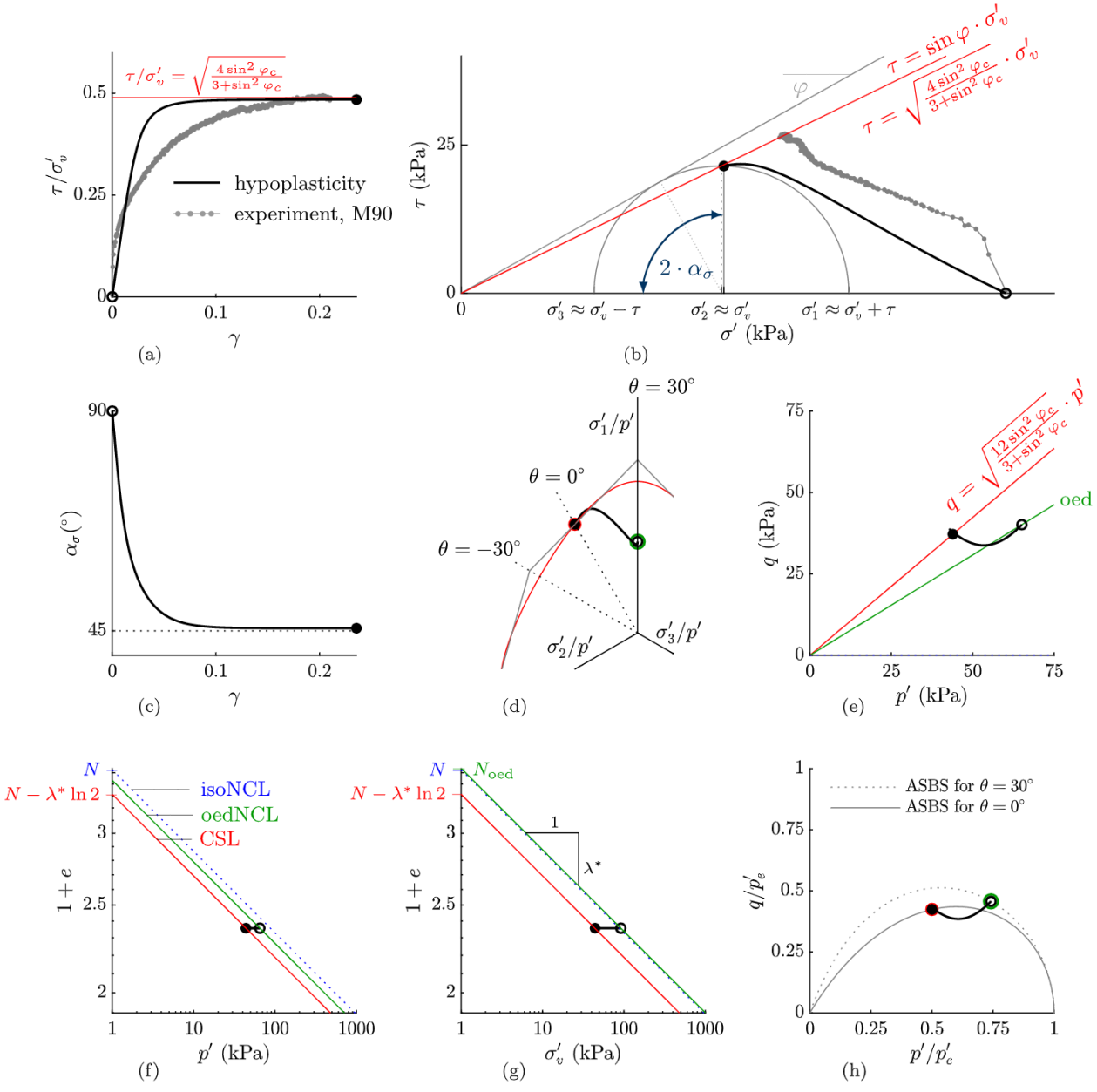

Fig. 5. Undrained simple shear test starting at oedometric normally consolidated state. Simulations with clay hypoplasticity, DSS test data (M90) from Laham et al. (2021).

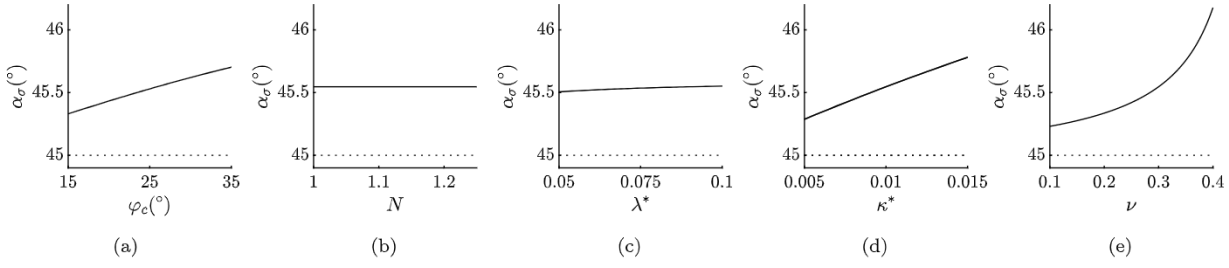

Fig. 6. In clay hypoplasticity, the principal stress direction α_σ at critical state slightly depends on the parameters of the material. In the Figs. (a)–(e) one parameter is varied, and the other parameters are chosen according to Table 1. As α_σ is close to 45° at critical state, 45° is a chosen as an approximation for the proposed calibration. The dotted line refers to a neglection of Zaremba/Jaumann expression, which yields $\alpha_\sigma = 45^\circ$ for any parameter combination.

Table 2
Calibration of clay hypoplasticity based on DSS and oedometric compression tests.

Parameter	Test	Determination
φ_c	DSS test	according to eq. (21): $\varphi_c = \arcsin\left(\sqrt{\frac{3\tau^2}{4\sigma_v'^2-\tau^2}}\right)$ with a pair of σ_v' and τ from DSS data at critical state
N, λ^*, κ^*	Oedometric compression test	according to Fig. C.1 (b) in the Appendix Section and described by Mašín (2019), Kadlíček (2019) and Kadlíček et al. (2022); For an automatic calibration, the software *Excalibre* on Soilmodels.com can be used.
ν	DSS test	by parametric study according to Fig. C.2 and optionally Fig. C.3 (simulation of oedometric unloading)

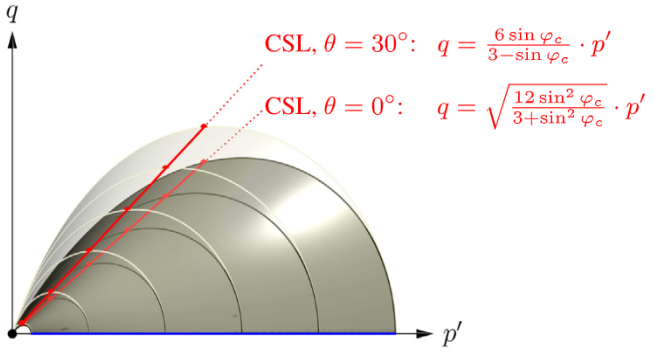

Fig. 7. Critical state lines for $\theta = 0°$ and $\theta = 30°$ and its related asymptotic state boundary surfaces. you can find an interactive graphic here.

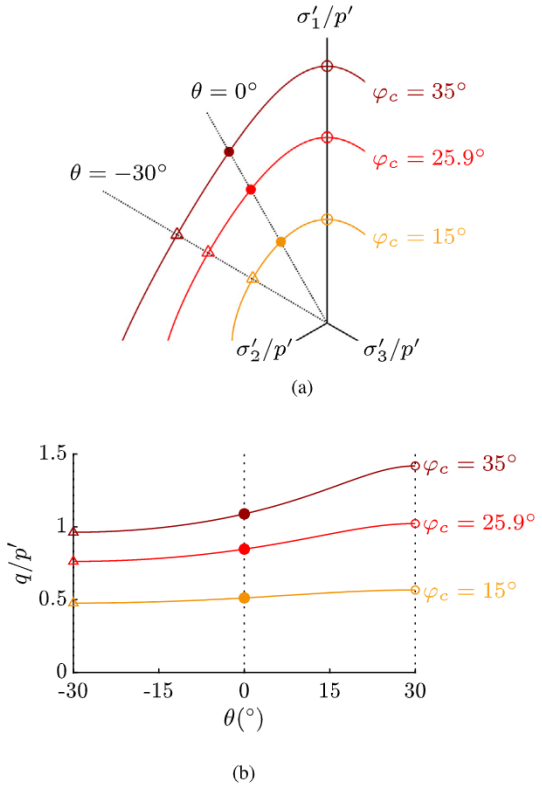

Fig. 8. Matsuoka–Nakai is shown for different values of φ_c in the normalized deviatoric plane in (a) as well as by q/p' for varying θ in (b).

critical stress ratio τ/σ_v' of the experiment is reached in the simulations with hypoplasticity, see Figs. 5 (a) and (b).

The slope of the CSL in $\tau - \sigma_v'$ plane in terms of the Matsuoka–Nakai critical friction angle φ_c reads as follows:

$$\frac{\tau}{\sigma_v'} = \sqrt{\frac{4\sin^2\varphi_c}{3+\sin^2\varphi_c}} \tag{22}$$

Eqs. (21) and (22) can be applied to clay hypoplasticity and for any constitutive model that predicts a stress rotation of major principal stress to the horizontal direction of 45° and reaches $\theta = 0°$ at critical state under DSS conditions.

Table 2 summarizes the calibration of clay hypoplasticity based on an undrained direct simple shear and on an oedometric compression test. For the calibration procedure of the parameters N, λ^*, κ^* and ν, we refer to Kadlíček et al. (2022) and Appendix C.

4.3.4. Principal stress state at critical state

With $b = 1/2$ in Eqs. (12), (13), (14) it follows that the principal stresses at critical state under DSS conditions can be described with τ and σ_v', see also Fig. 5(b):

$$\sigma_1' = \sigma_v' + \tau \tag{23}$$
$$\sigma_2' = \sigma_v' \tag{24}$$
$$\sigma_3' = \sigma_v' - \tau \tag{25}$$

Eqs. (23)–(25) lead to a critical stress state of a simple shear test simulated with clay hypoplasticity such that

$$p' = \sigma_v' \quad . \tag{26}$$

The fact that p' coincides with σ_v' at critical state is consistent with recent DEM direct simple shear investigations by Nguyen et al. (2021). In clay hypoplasticity, Eq. (26) is again based on the stress rotation of 45° at critical state and on the fact that the Lode angle θ equals 0° at plane strain critical state.

4.3.5. CSL in $e - \sigma_v'$ plane

By using $p' = \sigma_v'$ (Eq. (26)) for the CSL as defined in Eq. (B.2), we introduce the critical void ratio in dependence of σ_v':

$$\ln(1+e_c) = N - \lambda^* \ln\frac{2\sigma_v'}{\sigma^*} \tag{27}$$

To formulate the CSL under DSS conditions in σ_v'–e plane is useful when validating the CSL with experimental DSS data. The ordinate intercept of the CSL in the $\ln p' - \ln(1+e)$ and $\ln\sigma_v' - \ln(1+e)$ plots coincides with $N - \lambda\ln 2$ for $\sigma^* = 1$ kPa, see Fig. 5(f) and (g). However, Chen and Olson (2021) concluded that the ordinate intercepts of the CSL in $\ln p' - (1+e)$ and $\ln\sigma_v' - (1+e)$ planes differ and this is because of their assumption that the horizontal plane is the plane where the ratio of shear stress to normal stress is a maximum, whereas in clay hypoplasticity the horizontal plane corresponds to maximum shear stress. In addition, Chen and Olson assumed an axisymmetric principal stress state ($\theta = 30°$) at critical state under DSS conditions, whereas in clay hypoplasticity θ equals 0°.

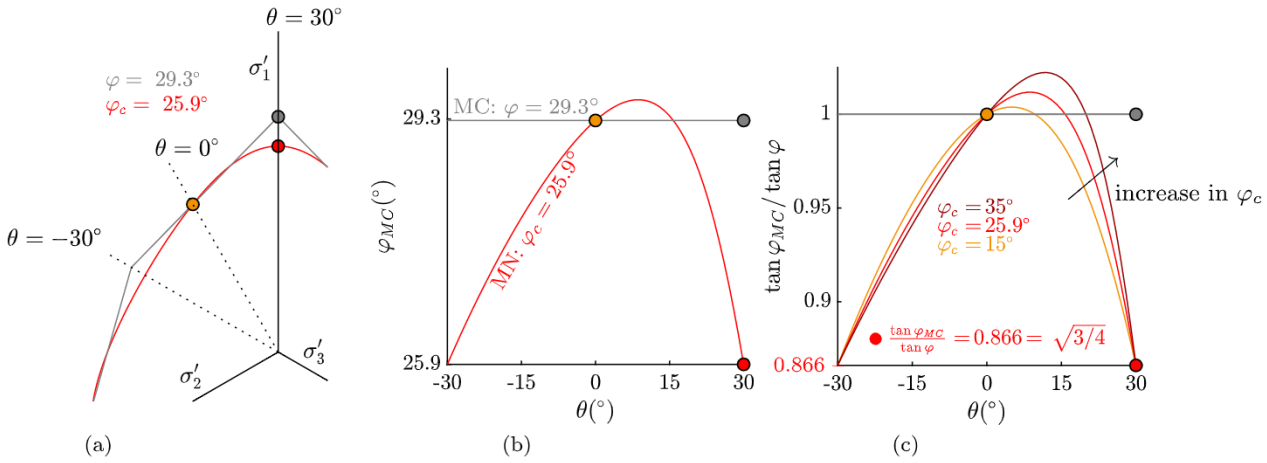

Fig. 9. Difference between Matsuoka–Nakai (MN) and Mohr–Coulomb (MC), when Matsuoka–Nakai and Mohr–Coulomb coincide for $\theta = 0°$. (a) deviatoric plane, (b) mobilized friction angles for $-30° < \theta < 30°$ for $\varphi_c = 25.9°$ and $\varphi = 29.3°$. (c) $\tan\varphi_{MC}/\tan\varphi$ for $-30° < \theta < 30°$ for varying φ_c and φ. This figure is inspired by the investigations by Griffiths and Huang (2009).

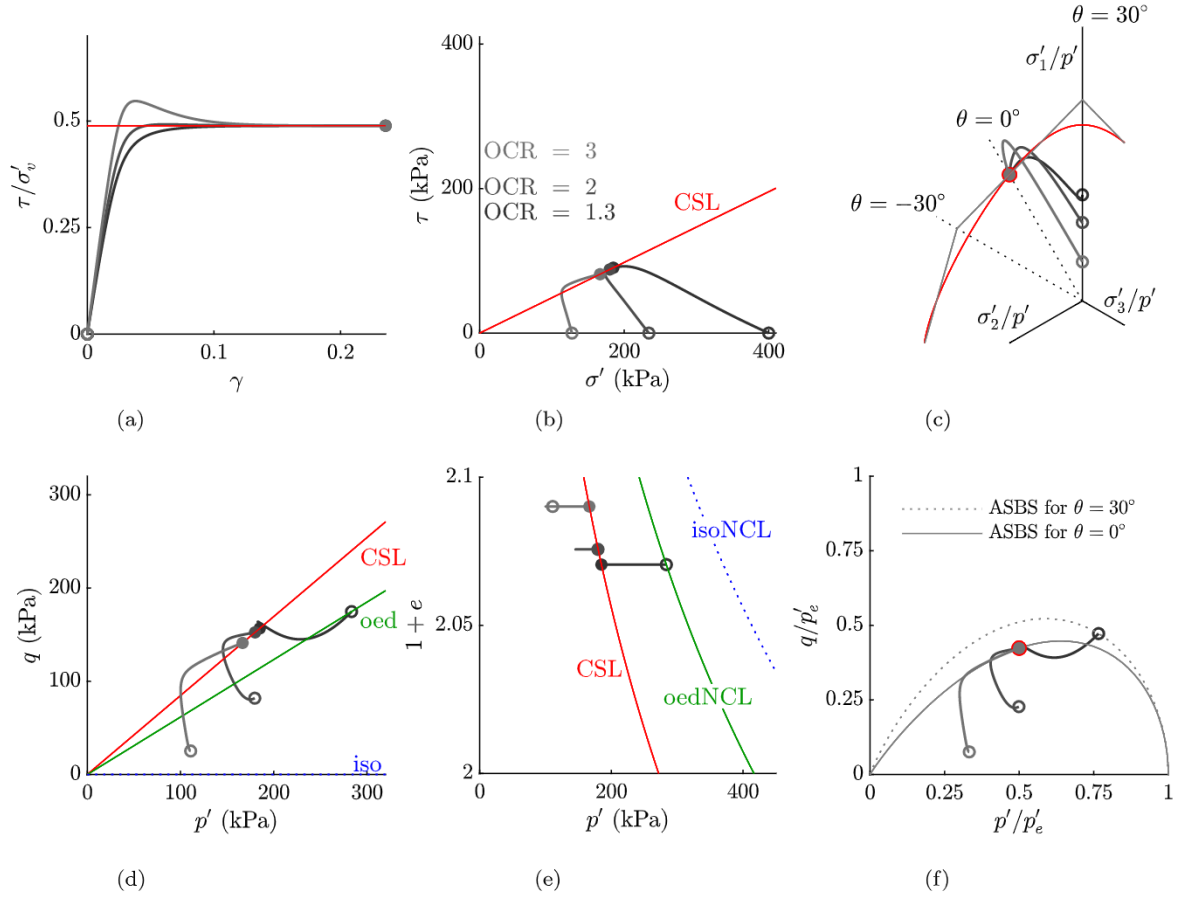

Fig. 10. Undrained simple shear test with different initial OCRs starting from different initial stress state. OCR = 1.3 refers to oedometric normal compression state. The circles (○) denote initial states, the bullets (•) denote critical states.

4.3.6. Slope of CSL in $p' - q$ plane for $\theta = 0°$

The Matsuoka–Nakai failure criterion can be expressed in terms of p', q and θ, see e.g. Griffiths and Huang (2009):

$$f = -\sqrt{2}K_{\mathrm{MN}}\sin(3\theta)t^3 + (9 - 3K_{\mathrm{MN}})t^2 s + (2K_{\mathrm{MN}} - 18)s^3 = 0 \tag{28}$$

with $s = -\sqrt{3}p'$ and $t = \sqrt{2/3}q$ and the material constant K_{MN}. The stress ratio q/p' for the Lode angle $\theta = 0°$ follows from Eq. (28), see also Figs. 5 (e) and 7:

$$\left(\frac{q}{p'}\right)_{\mathrm{MN}} = \frac{3}{\sqrt{2}} \cdot \sqrt{\frac{18 - 2K_{\mathrm{MN}}}{9 - 3K_{\mathrm{MN}}}} = \sqrt{\frac{12\sin^2\varphi_c}{3 + \sin^2\varphi_c}} \tag{29}$$

In Fig. 7 the asymptotic state boundary surfaces for $\theta = 0°$ (solid surface) and $\theta = 30°$ (transparent surface) are displayed. The surfaces include the critical state lines for $\theta = 0°$ and $\theta = 30°$ (axisymmetric triaxial compression). The Figure is linked to an interactive graphic,

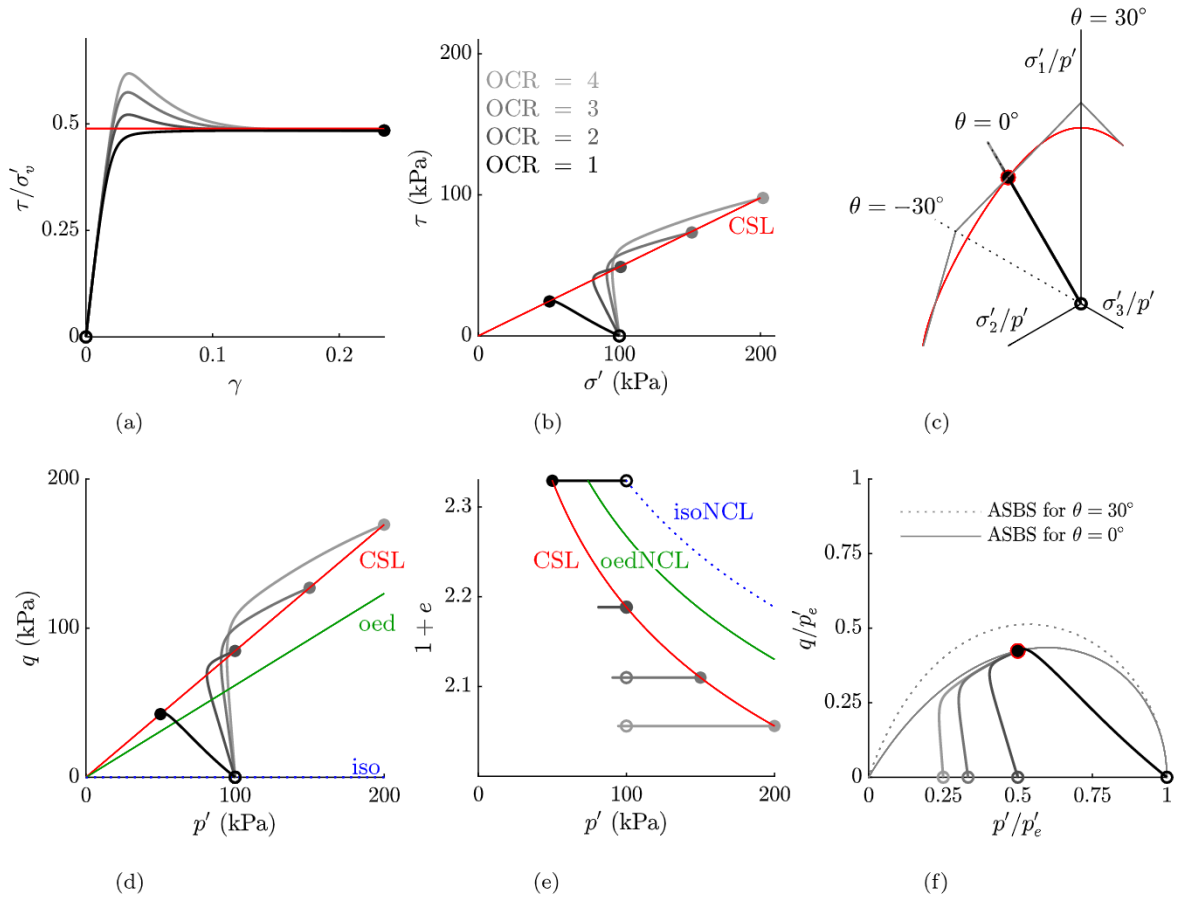

Fig. 11. Undrained simple shear test with different initial OCRs starting from hydrostatic stress state. The circles (∘) denote initial states, the bullets (•) denote critical states.

where it becomes visible that the CSLs overlap in the $p' - (1 + e)$ projection.

4.3.7. Sensitivity of φ_c on predicted strength

The stress paths followed by soil elements around a foundation subjected to combined loading can vary in direction (Andersen, 2009). On one hand, it is possible to predict the soil strength in all directions based on DSS results, as Matsuoka–Nakai is then fully characterized. On the other hand, any underestimation or overestimation of the friction angle along the DSS direction can be amplified along another direction. Consequently, a bespoke calibration procedure must be followed to improve design reliability and accuracy. Fig. 8 shows Matsuoka–Nakai for different values of φ_c. In Fig. 8(b) the stress ratio q/p' is displayed for different deviatoric directions. For triaxial extension (where $\theta = -30°$), q/p' is $6\sin\varphi_c/(3 + \sin\varphi_c)$, for triaxial compression ($\theta = 30°$), q/p' is $6\sin\varphi_c/(3 - \sin\varphi_c)$, for $\theta = 0°$, q/p' is given by Eq. (29). The stress ratios q/p' are possible final states that can be reached at critical state. A variation $\Delta\varphi_c = \text{const}$ has a higher impact on $\Delta(q/p')$ at triaxial compression (where $\theta = 30°$) than at lower values of θ. This is more pronounced for higher values of φ_c as the shape of Matsuoka–Nakai changes with changing φ_c: For very low values of φ_c the deviatoric shape of Matsuoka–Nakai is rather circular and becomes triangular for $\varphi_c = 90°$. For example a variation of $\Delta\varphi_c = 5°$ (from 30° to 35°) results in $\Delta(q/p') = 0.11$ at triaxial extension, $\Delta(q/p') = 0.13$ at $\theta = 0°$ and in $\Delta(q/p') = 0.22$ at $\theta = 30°$.

4.3.8. Comparison of friction angles from using Matsuoka–Nakai and Mohr–Coulomb

In soil modelling, the friction angle often refers to the Mohr–Coulomb failure criterion. We therefore give a short comparison between Matsuoka–Nakai and Mohr–Coulomb with a focus on the deviatoric direction $\theta = 0°$. The friction angle φ refers to Mohr–Coulomb, the critical friction angle φ_c refers to Matsuoka–Nakai. For a Lode angle of $\theta = 0°$, the Mohr–Coulomb failure condition is, c.f. Griffiths (1990):

$$\left(\frac{q}{p'}\right)_{\text{MC}} = \sin\varphi\sqrt{3} \tag{30}$$

Setting $(q/p')_{\text{MC}} = (q/p')_{\text{MN}}$ (Eqs. (29) and (30)) yields K_{MN} in terms of the Mohr–Coulomb friction angle φ (Eq. (1)):

$$K_{\text{MN}} = \frac{9 - 3\sin^2\varphi}{1 - \sin^2\varphi} \tag{31}$$

and with Eq. (5), we obtain

$$\sin^2\varphi_c = \frac{3\sin^2\varphi}{4 - \sin^2\varphi} \tag{32}$$

From applying the trigonometric expression for $\sin^2 x = \tan^2 x/(1 + \tan^2 x)$, we get:

$$\frac{\tan\varphi_c}{\tan\varphi} = \sqrt{\frac{3}{4}} \approx 0.866 \tag{33}$$

From Eq. (33) the Matsuoka–Nakai equivalent friction angle φ_c can be obtained from the Mohr–Coulomb friction angle φ for $\theta = 0°$, which coincides with plane-strain critical stress state conditions in clay hypoplasticity.

Fig. 9 shows that the difference between the shapes of Mohr–Coulomb and Matsuoka–Nakai. The friction angles are chosen in order that predictions coincide for the Lode angle $\theta = 0°$. Fig. 9(a) shows a deviatoric plane with intersections of the cone according to Matsuoka–Nakai for $\varphi_c = 25.9°$ superimposed on the Mohr–Coulomb hexagon where $\varphi = 29.3°$. Triaxial axisymmetric compression ($\theta = 30°$) and $\theta = 0°$ are marked with bullets. In Fig. 9(b), the stress states of the Matsuoka–Nakai surface are displayed for $-30° \le \theta \le 30°$ by the

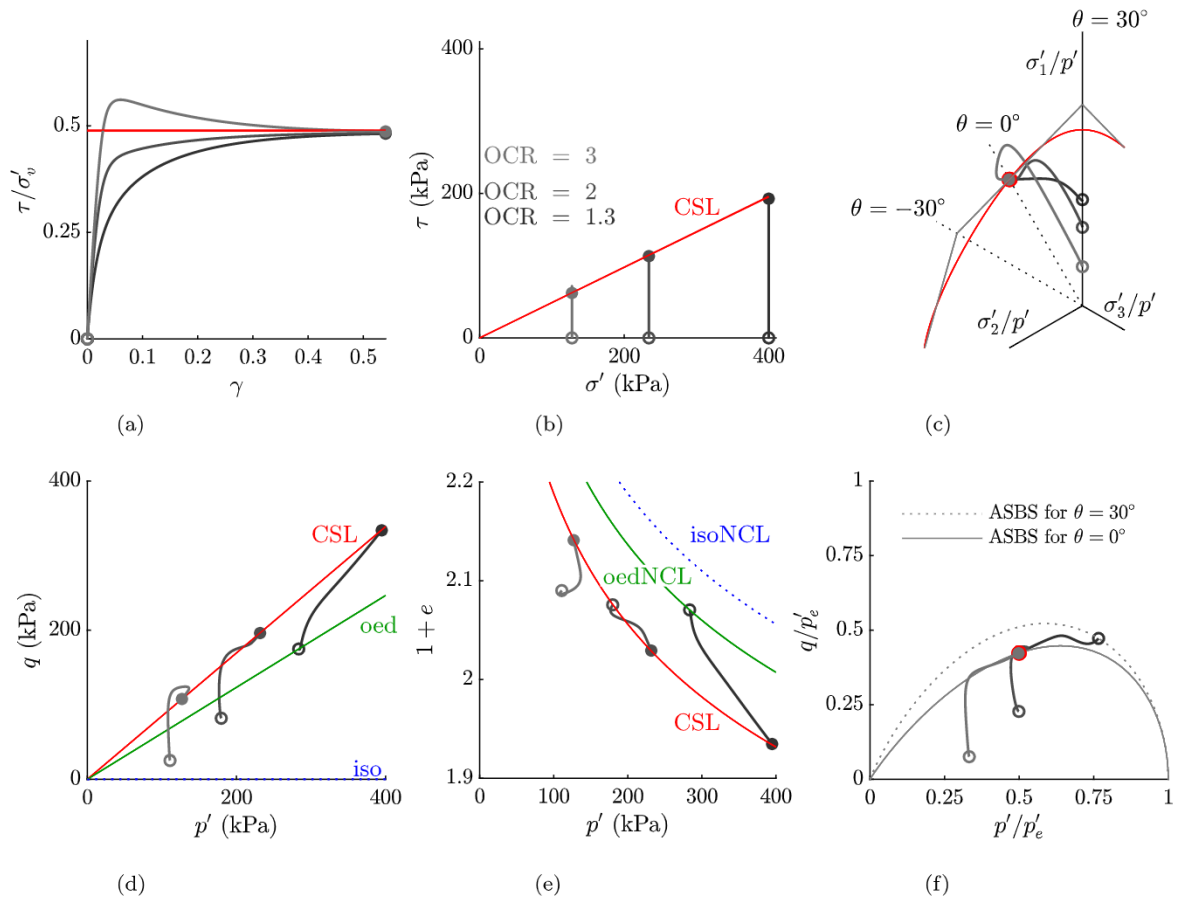

Fig. 12. Drained simple shear test with different initial OCRs starting from different initial stress state. OCR = 1.3 refers to oedometric normal compression state. The circles (∘) denote initial states, the bullets (•) denote critical states.

MC friction angle $\varphi_{MC} = \arcsin\left(\frac{\sigma_1'-\sigma_3'}{\sigma_1'+\sigma_3'}\right)$. For almost all deviatoric directions, Mohr–Coulomb exceeds Matsuoka–Nakai. A calibration of φ based on triaxial axisymmetric compression data would result in a lower value for MC according to e.g. Wood (1990). This implies that a constant value of φ cannot sufficiently describe strength predictions for all deviatoric directions. However, critical stress states in principal stress space can be well approximated with the Matsuoka–Nakai failure criterion (Nakai, 2007). Therefore, the Matsuoka–Nakai equivalent friction angle φ_c, which is included in hypoplasticity, is sufficient to describe critical strength predictions for different deviatoric directions. A change of φ_c affects the shape of Matsuoka–Nakai surface, see Fig. 9 (c). However, when comparing Matsuoka–Nakai with Mohr–Coulomb, the ratio $\frac{\tan\varphi_c}{\tan\varphi} = \sqrt{3/4} = 0.866$ is still constant for $\theta = 0°$.

The main outcomes of this section related to Critical State Soil Mechanics are summarized in the equations presented in Appendix D.

4.4. Influence of initial stress state and OCR

In this section, we show how a change in initial OCR or in initial stress state affects the DSS predictions with clay hypoplasticity. This highlights how potential initial error on the selected OCR can affect the results. We investigate stress paths and show that different to critical state predictions, the Lode angle at peak state is state-dependent, i.e. it depends on the initial OCR and initial stress state. The initial states in the simulations in Figs. 10 (undrained DSS) and 12 (drained DSS) have been chosen as follows: All samples have been oedometrically preconsolidated to $\sigma_v' = 400$ kPa. The sample with OCR = 1.3 is oedometrically normally consolidated. The samples with OCR = 2 and 3 respectively have then been oedometrically unloaded until $p_e'/p' = 2$ and 3 are reached.

In Figs. 11 (undrained DSS) and 13 (drained DSS), the initial stress state is hydrostatic with $\sigma_v' = p' = 100$ kPa and the initial OCR is varied from 1 to 4.

4.4.1. Undrained response

Fig. 10 shows simulations of undrained DSS tests with different initial OCRs. As expected, the stiffness and stress-ratio τ/σ_v' increases with increasing OCR, see Fig. 10 (a) and a higher initial OCR results in a higher stress ratio τ/σ_v'. The stress paths for samples with OCRs of 2 and 3 in Figs. 10 (b), (c) and (d) exceed the locus of critical stress state and again approach a Lode angle of 0° at critical state, see Figs. (c) and (f). At peak state, different Lode angles are reached for the different stress paths, see Fig. (c).

Fig. 11 shows simulations of undrained DSS test with initial OCRs from 1 to 4 with the same initial stress state $p' = \sigma_v' = 100$ kPa. The response in Fig. 11 is similar to the simulations in Fig. 10 and it is interesting to note that the stress paths in Fig. 11 (c) follow straight lines in the normalized deviatoric plane, i.e. the Lode angle stays 0° throughout all the simulations.

4.4.2. Drained response

Fig. 12 compares the simulated drained response of simple shear tests with different initial OCRs. Again, the sample with an OCR = 1.3 represents an oedometric normally consolidated sample. The stress ratio τ/σ_v' - shear strain response γ is displayed in Fig. 12(a) and the stress path in the τ–σ' plot is in (b). The related stress path in Fig. 12(c) in the normalized deviatoric plane is very similar to the undrained response (Fig. 10 c). The Lode angles at peak states differ and at critical state all stress paths again reach the Lode angle of 0°. The stress paths in $p' - q$ plane all show an increase in mean effective stress while σ_v' is

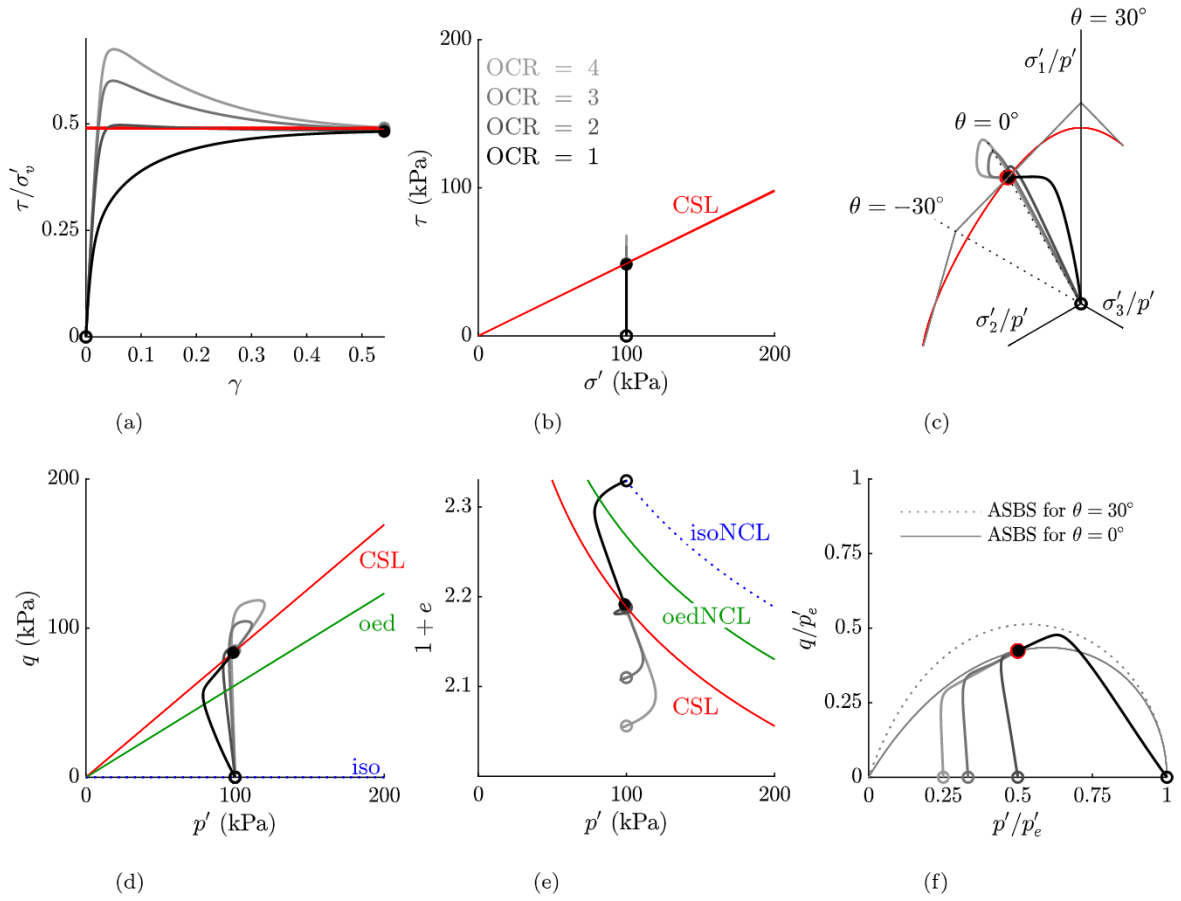

Fig. 13. Drained simple shear test with different initial OCRs starting from hydrostatic stress state. The circles (∘) denote initial states, the bullets (•) denote critical states.

kept constant, see Figs. 12 (b) and (d). In Fig. 12(e) the void ratio, mean effective stress response is displayed. Fig. 12(f) shows the asymptotic state boundary surface for $\theta = 30°$ including the oedometric normally consolidated state (where the initial state is marked with a ∘) and the ASBS for $\theta = 0°$ with the final critical state (marked with a •).

Fig. 13 shows simulations of drained DSS tests with $\sigma'_v = 100\,\text{kPa}$ = const. starting from different initial OCRs. Unlike the undrained response in the normalized deviatoric plane in Fig. 11 (c), the drained stress paths are curved in the normalized deviatoric plane in Fig. 13(c).

5. Summary and conclusion

In this article, we introduce analytical, Lode angle dependent approaches to determine Matsuoka–Nakai equivalent friction angles from DSS data. In order to apply the proposed calibration procedure to clay hypoplasticity, we investigate its direct simple shear response based on single element test simulations. The interpretation of clay hypoplasticity under DSS conditions in the framework of Critical State Soil Mechanics is feasible:

(i) Critical states in principal stress space are asymptotic states and thus the critical stress ratio q/p' is independent of the initial stress state and initial OCR. At critical states, the corresponding principal stress state lies on the critical stress locus according to Matsuoka–Nakai with the deviatoric direction $\theta = 0°$.

(ii) The inclination of major principal stress to the horizontal direction is approximately 45° at the critical state, i.e. the horizontal plane corresponds to maximum shear stress.

(iii) Based on both findings, (i) the Lode angle $\theta = 0°$ at critical state and (ii) the stress rotation of 45° at critical state, we explain the determination of the Matsuoka–Nakai equivalent critical friction angle φ_c from DSS experimental data: With σ'_v and τ at critical state, we obtain $\varphi_c = \arcsin\left(\sqrt{\frac{3\tau^2}{4\sigma_v'^2 - \tau^2}}\right)$ for clay hypoplasticity. This equation is also consistent with any constitutive model including Matsuoka–Nakai, if for its DSS critical state predictions, the horizontal plane corresponds to maximum shear stress and the principal stress state reaches $\theta = 0°$.

(iv) Points (i) and (ii) imply that the mean effective stress p' equals the vertical stress σ'_v at critical state. Demonstrating this, enabled us to show that the slope and ordinate intercepts of the critical state line in $\ln p' - \ln(1+e)$ and $\ln \sigma'_v - \ln(1+e)$ planes coincide for clay hypoplasticity.

A simple calibration procedure for the Matsuoka–Nakai equivalent friction angle, from DSS experimental data has been proposed. The proposed calibration can be applied for other constitutive models including the failure surface according to Matsuoka–Nakai. It results in realistic critical strength predictions and can be used to gain a better understanding in the numerical modelling of the complex stress states that result for example around offshore foundations.

CRediT authorship contribution statement

Gertraud Medicus: Developed the main concept of the manuscript, Performed the calculations and analyses, Mainly wrote the manuscript with input from all authors. **Katherine A. Kwa:** Developed the main concept of the manuscript, Curated the experimental data and wrote the text related to it, Reviewed and edited the manuscript. **Benjamin Cerfontaine:** Developed the main concept of the manuscript, Reviewed and edited the manuscript.

Declaration of competing interest

The authors declare that they have no known competing financial interests or personal relationships that could have appeared to influence the work reported in this paper.

Acknowledgements

This research was funded in part, by the Austrian Science Fund (FWF) V 918. For the purpose of open access, the authors have applied a CC BY public copyright licence to any Author Accepted Manuscript version arising from this submission. G.M. was further funded by the Austrian Science Fund (FWF): P 28934 and is grateful for the support of the University of Innsbruck: ProLehre Project *Animating Soil Models*: soilmodels.com/soilanim, AURORA Challenge Domains. K.K is funded by The Royal Academy of Engineering Chair in Emerging Technologies for Intelligent & Resilient Ocean Engineering and the EPSRC Supergen Offshore Renewable Energy (ORE) Hub (EP/S000747/1).

Appendix A. Symbols and notation

We use $\boldsymbol{\sigma}$ for Cauchy effective stress and $\mathbf{D}$ for stretching. Stress and strain are defined as positive for compression. Tensors are written in bold capital letters (e.g., $\mathbf{X}$). $\mathring{\boldsymbol{\sigma}}$ is the objective[3] (co-rotational) stress rate resulting from hypoplasticity, and $\dot{\boldsymbol{\sigma}}$ is the time derivative according to Zaremba/Jaumann (Zaremba, 1903), which is obtained by $\dot{\boldsymbol{\sigma}} = \mathring{\boldsymbol{\sigma}} + \mathbf{W}\boldsymbol{\sigma} - \boldsymbol{\sigma}\mathbf{W}$, with $\mathbf{W}$ being the antimetric part of the velocity gradient.

The stretching tensor $\mathbf{D}$ is the symmetric part of the velocity gradient. In general, stretching $\mathbf{D}$ is only approximately equivalent to the strain rate $\dot{\boldsymbol{\varepsilon}}$. For rectilinear extensions, $\mathbf{D}$ equals $\dot{\boldsymbol{\varepsilon}}$, with $\dot{\boldsymbol{\varepsilon}}$ being the logarithmic strain rate tensor.

The mean effective stress is $p' = \frac{1}{3}\operatorname{tr}\boldsymbol{\sigma}$, the deviatoric stress is

$$q = \left\{ \frac{1}{2}[(\sigma'_{22}-\sigma'_{33})^2+(\sigma'_{33}-\sigma'_{11})^2+(\sigma'_{11}-\sigma'_{22})^2]+3(\tau_{23}^2+\tau_{31}^2+\tau_{12}^2) \right\}^{1/2} .$$

In the simple shear investigations, the vertical stress σ'_{11} is denoted with σ'_v and the shear stress τ_{12} is denoted with τ (with $\tau_{23} = \tau_{31} = 0$). The associated shear strain γ_{12} is denoted with γ.

General stress states can be described by its principal values $\sigma'_1 \geq \sigma'_2 \geq \sigma'_3$ or by its stress invariants p', q and θ. The Lode angle θ defines the deviatoric direction of a stress state in the deviatoric plane. In this article, axisymmetric triaxial compression refers to the Lode angle $\theta = 30°$ and axisymmetric triaxial extension is described through $\theta = -30°$. Non-axisymmetric states are characterized by $-30° < \theta < 30°$. The Lode angle θ can be determined from $\theta = \arctan\left(\frac{1-2b}{\sqrt{3}}\right)$ with $b = \frac{\sigma'_3-\sigma'_2}{\sigma'_3-\sigma'_1}$. Alternatively, without the eigenvalues of $\boldsymbol{\sigma}$ being sorted, θ can be determined as follows: $\theta = \frac{1}{3}\arcsin\frac{3\sqrt{6}\det\boldsymbol{\sigma}^*}{\|\boldsymbol{\sigma}^*\|^3}$ with $\boldsymbol{\sigma}^* = \boldsymbol{\sigma} - \frac{\operatorname{tr}\boldsymbol{\sigma}}{3}\mathbf{1}$. The void ratio e is the ratio of the volume of the voids V_p to the volume of the solids V_s. The stress ratio $K = \sigma'_3/\sigma'_1$ at critical states equals K_c, and for oedometric normal compression K is denoted by K_0. In this article, φ refers to the Mohr–Coulomb (MC) hexagon. φ_c is used for Matsuoka–Nakai (MN) equivalent friction angle.[4] If a given critical stress state is described by φ_c, the equivalent Matsuoka–Nakai surface includes this particular stress state. As we compare critical strength predictions of Matsuoka–Nakai with Mohr–Coulomb, the cohesion c is always set equal to zero. In clay hypoplasticity, peak strength predictions are dependent on the initial overconsolidation ratio (OCR). The following definition of the OCR $= p'_e/p'$ is included in the mathematical formulation of clay hypoplasticity and used throughout the manuscript: the OCR is defined by means of the so-called *Hvorslev's equivalent consolidation pressure* $p'_e = \exp\left(\frac{N-\ln(1+e)}{\lambda^*}\right)$, divided by the actual mean stress p'. p'_e is the value of mean stress on the isotropic normal consolidation line which refers to the current specific volume $(1+e)$. N is the ordinate intercept, i.e. $N = \ln(1+e)$ at $p' = \sigma^* = 1$ kPa and λ^* is the slope of the NCL. The unloading stiffness under hydrostatic compression is described by the parameter κ^*.

Appendix B. Some concepts of clay hypoplasticity

The following concepts from Critical State Soil Mechanics relevant to this work, are included in the mathematical formulation of clay hypoplasticity:

- A critical stress state locus which is a line, the Critical State Line (CSL), in the $p'-q$ plot:

$$q = M \cdot p' \tag{B.1}$$

  with $M = 6\sin\varphi_c/(3-\sin\varphi_c)$ for axisymmetric triaxial compression, φ_c is the critical friction angle that can be calibrated from triaxial compression tests (undrained or drained), see also Mašín (2013). Kadlíček et al. (2022) propose to use undrained triaxial compression tests for clay. In three dimensional stress space, the critical stress locus according to Matsuoka and Nakai (1982) is included in the model.
- A stress-dependent critical void ratio e_c (CSL from Mašín, 2005) in the $p'-e$ plot, in order to distinguish between normally to slightly overconsolidated soil ($e > e_c$) and highly overconsolidated soil ($e < e_c$), see Fig. B.1(a):

$$\ln(1+e_c) = N - \lambda^* \ln\frac{2\,p'}{\sigma^*} \quad . \tag{B.2}$$

- The isotropic normal compression line (isoNCL) from Butterfield (1979), in order to define isotropic normally consolidated states:

$$\ln(1+e) = N - \lambda^* \ln\frac{p'}{\sigma^*} \quad , \tag{B.3}$$

  $\sigma^* = 1$ kPa is a reference stress, N and λ^* are soil parameters from Critical State Soil Mechanics.

Asymptotic states, including the isoNCL and CSL, can be displayed by the so-called asymptotic state boundary surface (ASBS), see Figs. B.1 (a), (b) and Mašín and Herle (2005). Figs. B.1 (a) and (b) are linked to interactive graphics.[5] Table 1 summarizes all parameters of Kaolin clay that are necessary for the calibration of clay hypoplasticity.

The cross section of the critical stress surface according to Matsuoka–Nakai in a deviatoric plane, which is obtained with clay hypoplasticity, is depicted in Fig. B.1 (c). The arrows denote different deviatoric directions of stretching. For a principal stress state, if the deviatoric direction of the stress state and strain increment coincide, then so-called *alignment* between deviatoric stress and deviatoric stretching exists, cf. Rauter et al. (2020) and Jop et al. (2006). Alignment applies for clay hypoplasticity, as investigated in Medicus (2020) and Medicus et al. (2021). The bold arrows in Fig. B.1 (c) indicate isochoric ($\operatorname{tr}\mathbf{D} = 0$) strain paths which are also plane-strain deformation states. The corresponding stress paths in principal stress space will therefore reach $\theta = 0°$ at critical states in clay hypoplasticity. Consequently, a Lode angle of $\theta = 0°$ implies that $\sigma'_2 = (\sigma'_1 + \sigma'_3)/2$.

The relationship between the deviatoric directions of stress states and strain increments can also be investigated experimentally. Nakai

[3] The term objectivity points to the fact that material behaviour is frame-indifferent, i.e., the behaviour is independent of the observers' motion.

[4] Generally in soil mechanics, φ_c is used for the critical state friction angle, which certainly can imply different deviatoric shapes of failure surfaces.

[5] The interactive WebGL graphics enable rotation and zoom and have been created using *Asymptote* vector graphic language: asymptote.sourceforge.io.

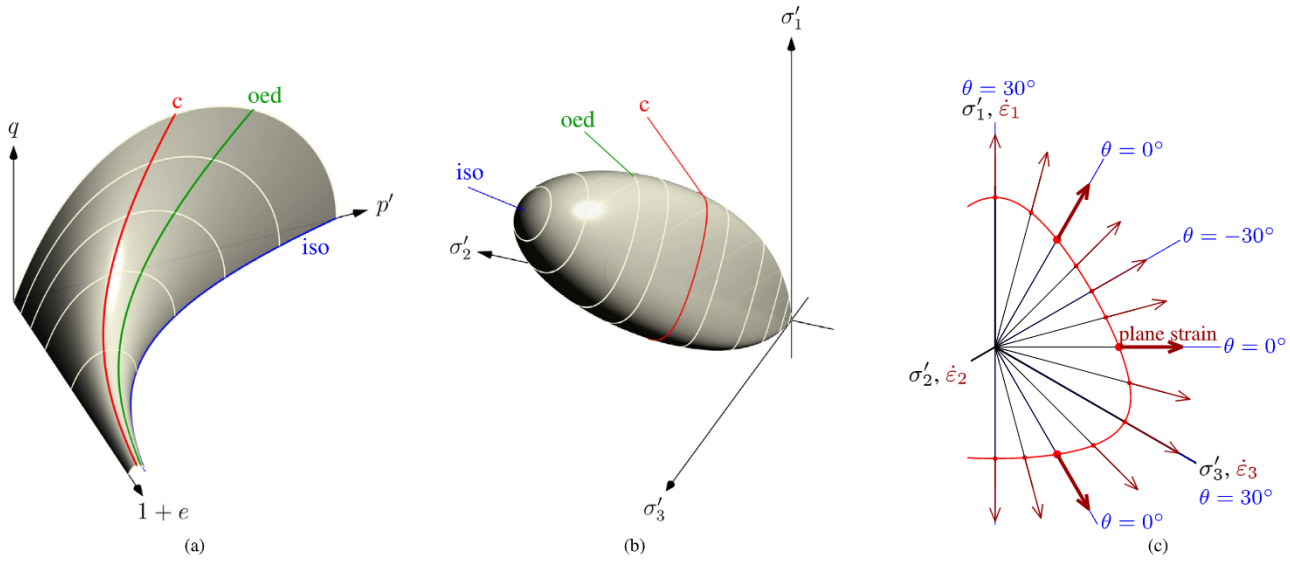

Fig. B.1. (a, b) So-called asymptotic state boundary surface of clay hypoplasticity; iso refers to hydrostatic compression, oed refers to oedometric compression and c refers to critical states. (a) p' - q - $(1+e)$ space for axisymmetric triaxial compression: you can find an interactive graphic here. (b) principal stress space: you can find an interactive graphic here. (c) Critical states in the deviatoric plane: *Alignment* between deviatoric stress and deviatoric stretching applies for clay hypoplasticity. The cross section of the critical stress surface according to Matsuoka–Nakai for $\varphi_c = 25.9°$ with a deviatoric plane is added, the arrows denote the deviatoric directions of stretching. The bold arrows denote isochoric plane-strain compression, which corresponds to a Lode angle $\theta = 0°$ at critical state.
Source: Fig. (c) is modified from Medicus et al. (2021).

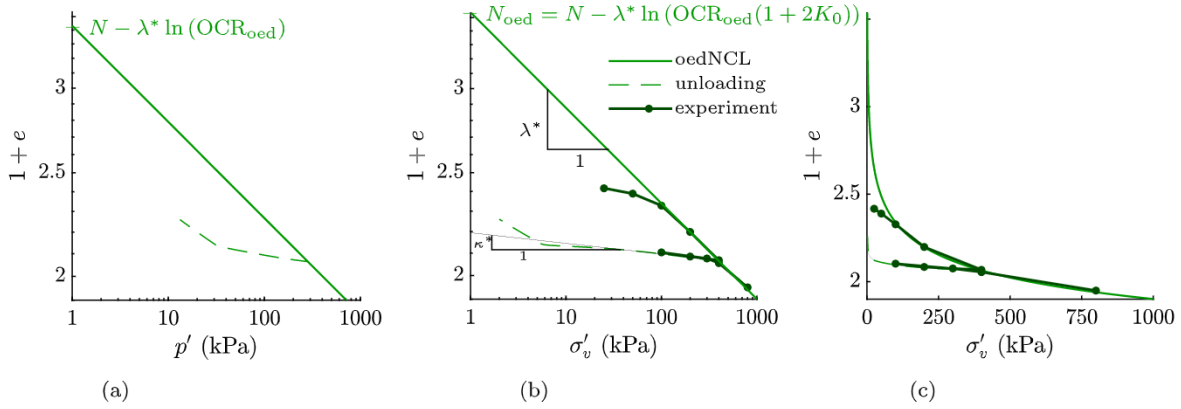

Fig. C.1. Oedometric compression test, oedNCL and unloading behaviour is simulated with hypoplasticity. (a) $\ln p' - \ln(1+e)$ plane. (b) $\ln \sigma'_v - \ln(1+e)$ plane. (c) $\sigma'_v - (1+e)$ plane: The sample (Oed01) is initially overconsolidated. Its path eventually approaches the oedNCL. Calibration of N_{oed} according to Eq. (C.3) and λ^* from loading, κ^* from unloading curve.

(2007) performed true triaxial tests on normally consolidated Fujinomori clay (with $p' = \text{const}$) with a fixed direction of each deviatoric stress path. Nakai (2007) observed only a small deviation between deviatoric stress and stretching at critical states. Similar conclusions were drawn by Yamada and Ishihara (1979) and Goldscheider (1976) from true triaxial tests on a sand material.

Appendix C. Calibration of N, λ^*, κ^* and ν

C.1. Normal compression lines and calibration of N and λ^*

Normal compression lines are formulated in $e-p'$ plane. From simple shear data generally only the vertical stress σ'_v is available as measure of the stress level.

In this section, normal compression lines are therefore formulated in dependence of σ'_v in order to make them comparable with experimental DSS data. The calibration of N and λ^* based on oedometric data can also be carried out with the calibration software ExCalibre (Kadlíček, 2019; Kadlíček and Mašín, 2020; Kadlíček et al., 2022), which is available on the platform SoilModels.com, see Gudehus et al. (2008).

Isotropic normal compression line (isoNCL). As $\sigma'_v = \sigma'_1 = \sigma'_2 = \sigma'_3 = p'$, the isoNCL in dependence of σ'_v reads

$$\ln(1+e) = N - \lambda^* \ln \frac{\sigma'_v}{\sigma^*} \tag{C.1}$$

The ordinate intercepts of the NCL in the $\ln p' - \ln(1+e)$ and $\ln \sigma'_v - \ln(1+e)$ plots thus coincide.

Oedometric normal compression line (oedNCL). The oedNCL is parallel to the isoNCL according to Gudehus et al. (2008), Mašín (2013), Kadlíček (2019) and Mašín (2019):

$$\ln(1+e_{oed}) = N - \lambda^* \ln \frac{\mathrm{OCR}_{oed} \cdot p'}{\sigma^*} \tag{C.2}$$

In the $\ln(1+e) - \ln \sigma'_v$ plane the oedNCL is also shifted compared with the isoNCL.

The ordinate intercept N_{oed} at $\sigma^* = 1$ kPa can be obtained from OCR_{oed} according to Eqs. (18)–(20) and from the mean stress $p' =$

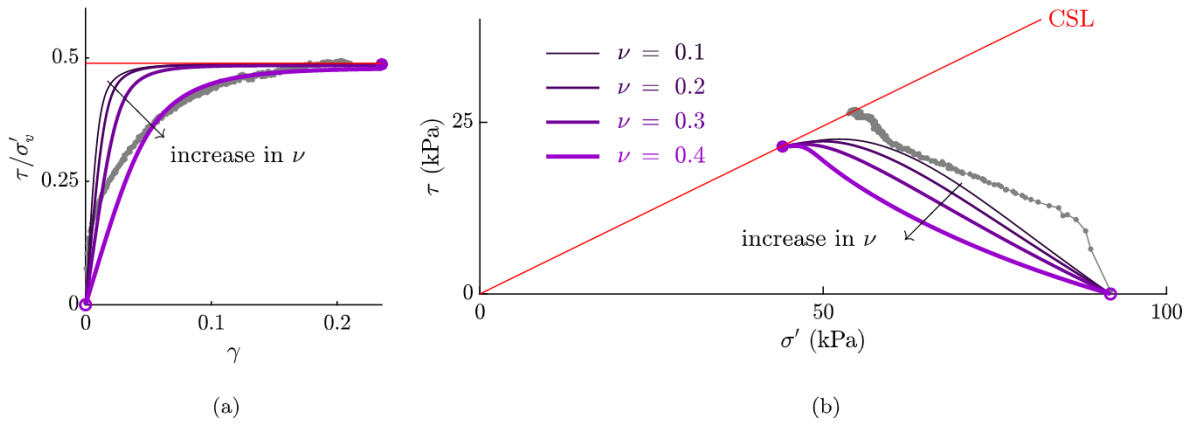

Fig. C.2. The parameter ν affects the shear stiffness (a) as well as the stress path (b) of an undrained simple shear test; ν can be obtained by parametric study. Simulations with hypoplasticity. Test data (M90) from Laham et al. (2021).

$\sigma'_v(1+2K_0)$ at K_0 state (see Figs. 5 (g) and C.1 (b)):

$$\ln(1+e_{\text{oed}}) = \underbrace{N - \lambda^* \ln\left(\text{OCR}_{\text{oed}}(1+2K_0)\right)}_{N_{\text{oed}}} \tag{C.3}$$

From Eq. (C.3) it can be seen that the ordinate intercepts in the $\ln p' - \ln(1+e)$ and $\ln \sigma'_v - \ln(1+e)$ plots differ as shown in see Figs. C.1 (a) and (b).

Figs. C.1 (b) and (c) include Kaolin data of an oedometric compression test: The sample is initially overconsolidated and eventually approaches the oedNCL. Once the $\ln \sigma'_v - \ln(1+e)$ response follows a straight line, the sample is presumed to be normally consolidated on the oedNCL and thus N and λ^* can be calibrated. N is obtained from Eq. (C.3).

C.2. Oedometric unloading and calibration of κ^*

According to Critical State Soil Mechanics, the unloading stiffness can be described by the parameter κ^* according to Eq. (C.4):

$$\ln(1+e) = N - \lambda^* \ln \frac{p'_0}{\sigma^*} + \kappa^* \ln \frac{p'_0}{p'} \tag{C.4}$$

where p'_0 is a preloading pressure on the isoNCL. For unloading, derivation of Eq. (C.4) with respect to time, t, yields:

$$\frac{\dot{e}}{1+e} = -\kappa^* \frac{\dot{p}'}{p'} \tag{C.5}$$

Oedometric unloading (and reloading) are governed by the parameter κ^* and, contrary to oedometric normal compression states, these stress paths do not follow a proportional stress path, i.e. a straight line in stress space. Therefore, transferring the unloading line from $\ln(1+e) - \ln p'$ to $\ln(1+e) - \ln \sigma'_v$ does not only result in a shift in $\ln(1+e)$ and can be fitted according to Fig. C.1(b). The unloading line of the oedometric compression test is displayed with the dashed line in Fig. C.1. The parameter κ^* can be calibrated from the slope of the oedometric unloading line in the $\ln(1+e) - \ln \sigma'_v$ plane,[6] see Fig. 5(g).

$$\frac{\dot{e}}{1+e} = -\kappa^* \frac{\dot{\sigma}'_v}{\sigma'_v} \tag{C.6}$$

C.3. Calibration of ν

The parameter ν controls the shear modulus and has an effect on the sample's undrained stress path, see Mašín (2013, 2019). It can thus be calibrated by parametric study by simulation of the undrained simple shear test. In Fig. C.2, ν is varied from 0.1 to 0.4 and the effect of ν on shear stiffness and on the stress path is shown.

The value of ν has an effect on the shape of the unloading oedometric path as shown in Fig. C.3. In $p' - e$ plane (Fig. C.3 a), the parameter ν only affects the response for lower stresses. However, in stress space (Figs. C.3 b, c), the influence of ν is more pronounced: For the other parameters according to Table 1, the simulations for $\nu = 0.1 \ldots 0.3$ result in a reasonable response, as there is an increase of K_0 through unloading as observed by e.g. Sivakumar et al. (2002) and Kolymbas and Bauer (1993). Note that the simulation with $\nu = 0.4$ predicts a decrease of K_0 through unloading.

Appendix D. DSS critical state predictions with clay hypoplasticity

This appendix summarizes the main equations of the study related to the hypoplastic model. For DSS critical state predictions with clay hypoplasticity according to Mašín (2013), the following equations can be applied:

D.1. Principal stresses

The principal stresses at critical state can be expressed in terms of τ and σ'_v:

$$\begin{aligned} \sigma'_1 &= \sigma'_v + \tau \\ \sigma'_2 &= \sigma'_v \\ \sigma'_3 &= \sigma'_v - \tau \end{aligned}$$

D.2. Stress invariants

Thus, the following stress invariants p', q, θ can be formulated:

$$\begin{aligned} p' &= \sigma'_v \\ q &= \sqrt{3}\tau \\ \theta &= 0° \end{aligned}$$

D.3. Critical state line

The CSL is formulated in the stress planes $p' - q$ and $\tau - \sigma'_v$:

$$q = \sqrt{\frac{12\sin^2\varphi_c}{3+\sin^2\varphi_c}} \cdot p'$$

$$\tau = \sqrt{\frac{4\sin^2\varphi_c}{3+\sin^2\varphi_c}} \cdot \sigma'_v$$

[6] The $\ln p'$ - $\ln(1+e)$ formulation of the Modified Cam Clay model, results in $\dot{p}' = p'/\kappa^* \cdot \dot{\varepsilon}_v$ to describe unloading and reloading within the elastic range with a constant slope. Note that different to that, in clay hypoplasticity, the unloading line does not *strictly* follow a straight line, in the $\ln p' - \ln(1+e)$ nor in the $\ln \sigma'_v - \ln(1+e)$ plane, see Mašín (2019).

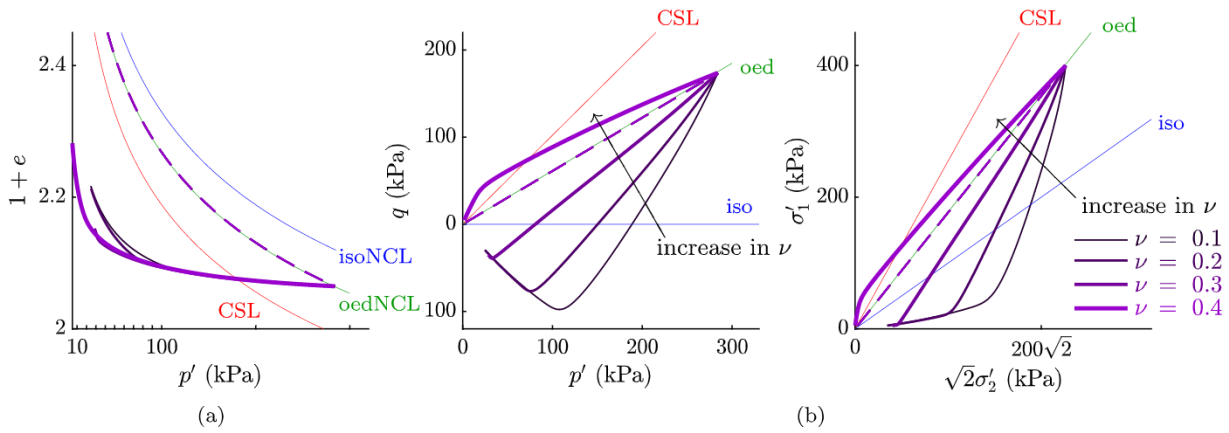

Fig. C.3. The parameter ν affects the unloading response in an oedometric compression test: The dashed line indicates loading, the solid lines refer to unloading. (a) $e - p'$ plane (b) stress paths in $p' - q$ plane and (c) Rendulic plane.

The critical friction angle φ_c can thus be determined from simple shear data τ and σ'_v at critical state:

$$\sin\varphi_c = \sqrt{\frac{3\tau^2}{4\sigma'^2_v - \tau^2}}$$

As $p' = \sigma'_v$ at critical state, the CSL in $\ln\sigma'_v - \ln(1+e)$ plane reads:

$$\ln(1+e_c) = N - \lambda^* \ln\frac{2\sigma'_v}{\sigma^*}$$

References

Andersen, K.H., 2009. Bearing capacity under cyclic loading—offshore, along the coast, and on land. The 21st bjerrum lecture presented in Oslo, 23 november 2007. Can. Geotech. J. 46 (5), 513–535.

Atkinson, J.H., Lau, W.H.W., Powell, J.J.M., 1991. Measurement of soil strength in simple shear tests. Can. Geotech. J. 28 (2), 255–262. http://dx.doi.org/10.1139/t91-031.

Bernhardt-Barry, M.L., Biscontin, G., O'Sullivan, C., 2021. Analysis of the stress distribution in a laminar direct simple shear device and implications for test data interpretation. Granul. Matter 23 (3), http://dx.doi.org/10.1007/s10035-021-01118-1.

Butterfield, R., 1979. A natural compression law for soils (An advance on e-log p'). Géotechnique 29 (4), 469–480.

Byrne, B.W., Houlsby, G.T., Burd, H.J., Gavin, K.G., Igoe, D.J., Jardine, R.J., Martin, C.M., McAdam, R.A., Potts, D.M., Taborda, D.M., et al., 2020. PISA design model for monopiles for offshore wind turbines: Application to a stiff glacial clay till. Géotechnique 70 (11), 1030–1047.

Chen, J., Olson, S.M., 2021. SHANSEP-based interpretation of overconsolidation effect on monotonic shearing resistance of contractive nonplastic soils. J. Geotech. Geoenviron. Eng. 147 (12), 04021155. http://dx.doi.org/10.1061/(ASCE)GT.1943-5606.0002680.

Dyvik, R., Berre, T., Lacasse, S., Raadim, B., 1987. Comparison of truly undrained and constant volume direct simple shear tests. Geotechnique 37 (1), 3–10. http://dx.doi.org/10.1680/geot.1987.37.1.3.

Fellin, W., 2011. Abschätzung der Standsicherheit von annähernd unendlich langen Kriechhängen. Geotechnik 34 (1), 22–31. http://dx.doi.org/10.1002/gete.201000018.

Goldscheider, M., 1976. Grenzbedingung und Fließregel von Sand. Mech. Res. Commun. 3, 463–468. http://dx.doi.org/10.1016/0093-6413(76)90037-9.

Grammatikopoulou, A., Zdravkovic, L., Potts, D.M., 2007. The effect of the yield and plastic potential deviatoric surfaces on the failure height of an embankment. Géotechnique 57 (11), 795–806, URL: http://www.icevirtuallibrary.com/;jsessionid=1ngc5r7k0xcrt.x-telford-live-01content/article/10.1680/geot.2007.57.10.795.

Griffiths, D.V., 1990. Failure criteria interpretation based on Mohr-Coulomb friction. J. Geotech. Eng. 116 (6), 986–999. http://dx.doi.org/10.1061/(ASCE)0733-9410(1990)116:6(986).

Griffiths, D.V., Huang, J., 2009. Observations on the extended Matsuoka–Nakai failure criterion. Int. J. Numer. Anal. Methods Geomech. 33 (17), 1889–1905. http://dx.doi.org/10.1002/nag.810.

Gudehus, G., Amorosi, A., Gens, A., Herle, I., Kolymbas, D., Mašín, D., Muir Wood, D., Nova, R., Niemunis, A., Pastor, M., Tamagnini, C., Viggiani, G., 2008. The soilmodels.info project. Int. J. Numer. Anal. Methods Geomech. 32, 1571–1572. http://dx.doi.org/10.1002/nag.675.

Gudehus, G., Mašín, D., 2009. Graphical representation of constitutive equations. Géotechnique 59 (2), 147–151. http://dx.doi.org/10.1680/geot.2007.00155.

Jerman, J., Mašín, D., 2021. Evaluation of hypoplastic model for soft clays by modelling of Nicoll highway case history. Comput. Geotech. 134, 104053. http://dx.doi.org/10.1016/j.compgeo.2021.104053.

Jop, P., Forterre, Y., Pouliquen, O., 2006. A constitutive law for dense granular flows. Nature 441, 727–730. http://dx.doi.org/10.1038/nature04801.

Kadlíček, T., 2019. Parameters Identification of Advanced Constitutive Models of Soils (Ph.D. thesis). Czech Technical University in Prague, URL: https://dspace.cvut.cz/handle/10467/83187.

Kadlíček, T., Janda, T., Šejnoha, M., Mašín, D., Najser, J., Beneš, v., 2022. Automated calibration of advanced soil constitutive models. Part II: Hypoplastic clay and modified Cam-Clay. Acta Geotech. http://dx.doi.org/10.1007/s11440-021-01435-y.

Kadlíček, T., Mašín, D., 2020. The strength reduction method in clay hypoplasticity. Comput. Geotech. 126, 103687. http://dx.doi.org/10.1016/j.compgeo.2020.103687.

Kinner, E.B., 1973. Undrained bearing capacity of footing on clay. In: Proc. of the 8th Int. Conf. on SMFE, Moscow, vol. 1, pp. 209–215.

Kolymbas, D., 1977. A rate-dependent constitutive equation for soils. Mech. Res. Commun. 4, 367–372. http://dx.doi.org/10.1016/0093-6413(77)90056-8.

Kolymbas, D., 2015. Introduction to barodesy. Géotechnique 65 (13), 52–65. http://dx.doi.org/10.1680/geot.14.P.151.

Kolymbas, D., Bauer, E., 1993. Soft oedometer — A new testing device and its application for the calibration of hypoplastic constitutive laws. Geotech. Test. J. 16 (2), 263–270.

Kolymbas, D., Herle, I., 2003. Shear and objective stress rates in hypoplasticity. Int. J. Numer. Anal. Methods Geomech. 27 (9), 733–744. http://dx.doi.org/10.1002/nag.297.

Lagioia, R., Panteghini, A., 2014. The influence of the plastic potential on plane strain failure. Int. J. Numer. Anal. Methods Geomech. 38 (8), 844–862. http://dx.doi.org/10.1002/nag.2236.

Laham, N.I., Kwa, K.A., White, D.J., Gourvenec, S.M., 2021. Episodic simple shear tests to measure strength changes for whole-life geotechnical design. Géotech. Lett. 11 (1), 103–111. http://dx.doi.org/10.1680/jgele.20.00124.

Liu, H., Kementzetzidis, E., Abell, J.A., Pisanò, F., 2021. From cyclic sand ratcheting to tilt accumulation of offshore monopiles: 3D FE modelling using SANISAND-MS. Géotechnique 1–16.

Matsuoka, H., Nakai, T., 1982. A new failure criterion for soils in three dimensional stress. In: IUTAM Conference on Deformation and Failure of Granular Materials. Delft, pp. 253–263.

Mašín, D., 2005. A hypoplastic constitutive model for clays. Int. J. Numer. Anal. Methods Geomech. 29 (4), 311–336. http://dx.doi.org/10.1002/nag.416.

Mašín, D., 2012. Asymptotic behaviour of granular materials. Granul. Matter 14, 759–774. http://dx.doi.org/10.1007/s10035-012-0372-x.

Mašín, D., 2013. Clay hypoplasticity with explicitly defined asymptotic states. Acta Geotech. 8 (5), 481–496. http://dx.doi.org/10.1007/s11440-012-0199-y.

Mašín, D., 2019. Modelling of Soil Behaviour with Hypoplasticity – Another Approach to Soil Constitutive Modelling. In: Springer Series in Geomechanics and Geoengineering, Springer International Publishing.

Mašín, D., Herle, I., 2005. State boundary surface of a hypoplastic model for clays. Comput. Geotech. 32 (6), 400–410. http://dx.doi.org/10.1016/j.compgeo.2005.09.001.

Mašín, D., Herle, I., 2007. Improvement of a hypoplastic model to predict clay behaviour under undrained conditions. Acta Geotech. 2, 261–268. http://dx.doi.org/10.1007/s11440-007-0043-y.

Mayne, P.W., 1985. A review of undrained strength in direct simple shear. Soils Found. 25 (3), 64–72.

Medicus, G., 2020. Asymptotic state boundaries and peak states in barodesy for clay. Géotech. Lett. 10 (2), 1–8. http://dx.doi.org/10.1680/jgele.19.00088.

Medicus, G., Bode, M., Tschuchnigg, F., Schneider-Muntau, B., 2021. Plane strain failure for different constitutive models. In: Barla, M., Di Donna, A., Sterpi, D. (Eds.), Challenges and Innovations in Geomechanics. Springer International Publishing, Cham, pp. 498–506. http://dx.doi.org/10.1007/978-3-030-64514-4_49.

Medicus, G., Fellin, W., 2017. An improved version of barodesy for clay. Acta Geotech. 12 (2), 365–376. http://dx.doi.org/10.1007/s11440-016-0458-4.

Nakai, T., 2007. Modeling of soil behavior based on t_{ij} concept. In: Proceedings of 13th Asian Regional Conference on Soil Mechanics and Geotechnical Engineering, ARCSMGE. Kolkata, vol. 2, pp. 69–89, Keynote Paper.

Nakai, T., Hinokio, M., 2004. A simple elastoplastic model for normally and over consolidated soils with unified material parameters. Soils Found. 44 (2), 53–70. http://dx.doi.org/10.3208/sandf.44.2_53.

Nguyen, H.B.K., Rahman, M.M., Fourie, A., 2021. The critical state behaviour of granular material in triaxial and direct simple shear condition: A DEM approach. Comput. Geotech. 138, 104325. http://dx.doi.org/10.1016/j.compgeo.2021.104325.

Nitzsche, K., Herle, I., 2014. Analysis of displacement patterns during an excavation using different constitutive models. In: Proceedings of the 8th European Conference on Numerical Methods in Geotechnical Engineering, NUMGE 2014, vol. 2, pp. 777–782.

Page, A.M., Klinkvort, R.T., Bayton, S., Zhang, Y., Jostad, H.P., 2021. A procedure for predicting the permanent rotation of monopiles in sand supporting offshore wind turbines. Mar. Struct. 75, 102813. http://dx.doi.org/10.1016/j.marstruc.2020.102813.

Potts, D.M., Zdravković, L., 1999. Finite Element Analysis in Geotechnical Engineering. Thomas Telford Publishing, http://dx.doi.org/10.1680/feaiget.27534.

Randolph, M., 2000. Effect of strength anisotropy on capacity of foundations. In: Effect of Strength Anisotropy on Capacity of Foundations. CRC Press/Balkema, pp. 313–327.

Rauter, M., Barker, T., Fellin, W., 2020. Granular viscosity from plastic yield surfaces: The role of the deformation type in granular flows. Comput. Geotech. 112, http://dx.doi.org/10.1016/j.compgeo.2020.103492.

Rowe, P.W., 1969. The relation between the shear strength of sands in triaxial compression, plane strain and direct shear. Géotechnique 19 (1), 75–86. http://dx.doi.org/10.1680/geot.1969.19.1.75.

Schranz, F., 2018. In: Kolymbas, D. (Ed.), Applications and Developments of Barodesy. In: Advances in Geotechnical Engineering and Tunnelling, (24), Logos Verlag Berlin.

Schranz, F., Fellin, W., 2015. Stability of infinite slopes investigated with elastoplasticity and hypoplasticity. Geotechnik http://dx.doi.org/10.1002/gete.201500021.

Sivakumar, V., Doran, I., Graham, J., Navaneethan, T., 2002. Relationship between K_0 and overconsolidation ratio: A theoretical approach. Géotechnique 52, 225–230. http://dx.doi.org/10.1680/geot.52.3.225.41017.

Sławińska-Budzich, J., 2021. Characteristic parameters of soil failure criteria for plane strain conditions – experimental and semi-theoretical study. Stud. Geotech. Mech. 43 (3), 237–254. http://dx.doi.org/10.2478/sgem-2021-0015.

Stutz, H., Mašín, D., Sattari, A.S., Wuttke, F., 2017. A general approach to model interfaces using existing soil constitutive models application to hypoplasticity. Comput. Geotech. 87, 115–127. http://dx.doi.org/10.1016/j.compgeo.2017.02.010.

Taiebat, M., Dafalias, Y.F., 2008. SANISAND: SImple anisotropic sand plasticity model. Int. J. Numer. Anal. Methods Geomech. 32 (8), 915–948. http://dx.doi.org/10.1002/nag.651.

Thornton, C., Zhang, L., 2006. A numerical examination of shear banding and simple shear non-coaxial flow rules. Phil. Mag. 86 (21–22), 3425–3452.

Tsegaye, A., Benz, T., Nordal, S., 2013. On the geometry of plastic potential surfaces and isochoric stress paths. In: Conference: ISSMGE, At: Paris.

Wichtmann, T., 2020. Soil behaviour under low- and high-cycle loading - element tests vs. constitutive models. Geomech. Energy Environ. http://dx.doi.org/10.1016/j.gete.2020.100188.

Wijewickreme, D., Dabeet, A., Byrne, P., 2013. Some observations on the state of stress in the direct simple shear test using 3D discrete element analysis. Geotech. Test. J. 36, 20120066. http://dx.doi.org/10.1520/GTJ20120066.

von Wolffersdorff, P.-A., 1996. A hypoplastic relation for granular materials with a predefined limit state surface. Mech. Cohesive-Frict. Mater. 1, 251–271. http://dx.doi.org/10.1002/(SICI)1099-1484(199607)1:3{<}251::AID-CFM13{>}3.0.CO;2-3.

Wood, D.M., 1990. Soil Behaviour and Critical State Soil Mechanics. Cambridge University Press.

Wood, D.M., 2004. Geotechnical Modelling. Spon Press, London.

Yamada, Y., Ishihara, K., 1979. Anisotropic deformation characteristics of sand under three dimensional stress conditions. Soils Found. 19, 97–107.

Yu, H.-S., 2006. Plasticity and Geotechnics. In: Advances in Mechanics and Mathematics, (1), Springer US, http://dx.doi.org/10.1007/978-0-387-33599-5.

Zaremba, S., 1903. Sur une forme perfectionee de la theorie de la relaxation. Bull. Int. Acad. Sci. Cracovie 594–614, URL: https://ci.nii.ac.jp/naid/10011562502/en/.

Zhang, L., 2003. The behaviour of granular material in pure shear, direct shear and simple shear (Ph.D. thesis). Aston University.